The Astronomical Journal, 161:149 (17pp), 2021 March https://doi.org/10.3847/1538-3881/abdd3b

Interstellar Extinction, Polarization, and Grain Alignment in the Sh 2-185 (IC 59 and IC 63) Region

Archana Soam[1], B-G Andersson[1], V. Straižys[2], Miranda Caputo[1,3], A. Kazlauskas[2], R. P. Boyle[4], R. Janusz[5], J. Zdanavičius[2], and J. A. Acosta-Pulido[6,7]
[1] SOFIA Science Center, USRA, NASA Ames Research Center, M.S. 232-12, Moffett Field, CA 94035, USA; asoam@usra.edu
[2] Institute of Theoretical Physics and Astronomy, Vilnius University, Saulėtekio al. 3, Vilnius, LT-10257, Lithuania
[3] Ritter Astrophysical Research Center, University of Toledo, Dept. of Physics and Astronomy, 2801 W. Bancroft St., Toledo, OH 43606, USA
[4] Vatican Observatory Research Group, Steward Observatory, Tucson, AZ 85721, USA
[5] Vatican Observatory, I-00120, Vatican City, Italy
[6] Instituto de Astrofísica de Canarias (IAC), C/O Via Lactea, s/n E-38205- La Laguna, Tenerife, Spain
[7] Departamento de Astrofísica, Universidad de La Laguna, E-38205 La Laguna, Tenerife, Spain
Received 2020 June 1; revised 2021 January 14; accepted 2021 January 15; published 2021 February 25

Abstract

Optical and infrared continuum polarization from the interstellar medium is driven by radiative processes aligning the grains with the magnetic field. While a quantitative, predictive theory of radiative alignment torques (RATs) exists and has been extensively tested, several parameters of the theory remain to be fully constrained. In a recent paper, Medan & Andersson showed that the polarization efficiency (and therefore grain alignment efficiency) at different locations in the wall of the Local Bubble (LB) could be modeled as proportional to the integrated light intensity from the surrounding stars and OB associations. Here we probe that relationship at high radiation field intensities by studying the extinction and polarization in the two reflection nebulae IC 59 and IC 63 in the Sh 2-185 H II region, illuminated by the B0 IV star γ Cassiopeia. We combine archival visual polarimetry with new seven-band photometry in the Vilnius system, to derive the polarization efficiency from the material. We find that the same linear relationship seen in the LB wall also applies to the Sh 2-185 region, strengthening the conclusion from the earlier study.

Unified Astronomy Thesaurus concepts: Interstellar dust (836); Starlight polarization (1571)

Supporting material: machine-readable tables

1. Introduction

The realization that interstellar polarization of stars is due to asymmetric dust grains, aligned with the magnetic field, has proven to be key for mapping the interstellar medium magnetic fields. Dust-induced interstellar polarization was first detected by Hall (1949) and Hiltner (1949a, 1949b). This effect has been used extensively to derive the magnetic field maps in different environments (e.g., Vrba et al. 1976; Hodapp 1987; Bhatt & Jain 1993; Pereyra and Magalhães 2002; Matthews et al. 2009; Chapman et al. 2011; Sugitani et al. 2011). Polarization of starlight at visible and near-infrared wavelengths is due to dichroic extinction by nonspherical dust grains that are aligned with their short axis parallel to the local magnetic field (Whittet & Dust 2003). Aligned dust grains can similarly emit polarized thermal radiation in the far-infrared and at (sub)millimeter wavelengths (e.g., Cudlip et al. 1982; Rao et al. 1998; Dotson et al. 2000; Vaillancourt & Matthews 2012).

The mechanism by which the dust grains align with the magnetic field has long been unclear. A long-assumed mechanism to account for the effect, based on paramagnetic relaxation in rapidly rotating grains (Davis & Greenstein 1951), has now been shown to be unviable in most instances both observationally (Hough et al. 2008) and theoretically (Lazarian & Draine 1999). However, a radiatively driven mechanism, originally proposed by Dolginov & Mitrofanov (1976) and more fully developed by Draine & Weingartner (1996) and Lazarian & Hoang (2007), has now become the generally assumed alignment mechanism. This "radiative alignment torque (RAT) theory" posits that grains are spun up by the transfer of torques from photons in an anisotropic radiation field to helical dust grains. For paramagnetic grains, the resultant rotation induces a magnetic moment through the Barnett effect (Purcell 1979). This induced magnetic moment will cause the grain's angular (and magnetic!) momentum vector to Larmor-precess around an external magnetic field. Continued RAT torques during the Larmor precession finally align the grain with the magnetic field. A large number of the predictions of this theory have been confirmed over the past decade (see Andersson et al. 2015; for a review), but details of the mechanism and its components still remain to be probed.

It is important to note that, in most environments, RAT alignment is magnetic alignment, i.e., the grains are aligned with their angular momentum vectors along the magnetic field, and the direction of the observed dichroic extinction polarization traces the plane of the sky projection of the field. Second-order effects—such as alignment along the radiation field direction, for very strong radiation fields (e.g. Kataoka et al. 2017; Lazarian & Hoang 2019), and the impact of non-paramagnetic grain materials (carbon solids; e.g., Andersson et al. 2018; B.-G. Andersson et al. 2020, in preparation)—can be important in rare, extreme environments.

While the principles of RAT grain alignment are now well established, we still need to understand the quantitative aspects of the grain alignment mechanism in the context of the strength of radiation and magnetic fields. Medan & Andersson (2019) presented a detailed study of the interstellar polarization due to dust in the Local Bubble (LB) wall (Lallement et al. 2003), investigating grain alignment and polarization efficiency dependence on radiation from OB and field stars. They used polarization measurements from Berdyugin et al. (2014)

Table 1
Results of Photometry and Classification of Stars in the Vilnius System for the IC 59 Stars with the Vatican Advanced Technology Telescope (VATT)

No.	R.A. (J2000) (hh:mm:ss)	Decl. (J2000) (dd:mm:ss)	V (mag)	$U-V$ (mag)	$P-V$ (mag)	$X-V$ (mag)	$Y-V$ (mag)	$Z-V$ (mag)	$V-S$ (mag)	$e(V)$ (mag)	$e(U-V)$ (mag)	$e(P-V)$ (mag)	$e(X-V)$ (mag)	$e(Y-V)$ (mag)	$e(Z-V)$, (mag)	$e(V-S)$ (mag)	Sp type	A_V (mag)	d (pc)
1	00:56:37.79	+61:07:49.5	16.341	—	2.867	1.963	0.896	0.313	0.859	0.012	—	0.033	0.017	0.013	0.016	0.013	f5 III	1.868	7008.0
2	00:56:38.76	+61:12:48.3	15.831	3.636	2.694	1.748	0.788	0.290	0.674	0.032	0.062	0.026	0.033	0.012	0.039	0.012	a6 IV	2.205	2170.0
3	00:56:43.71	+61:03:28.5	13.669	2.777	2.071	1.296	0.544	0.198	0.539	0.013	0.020	0.025	0.016	0.014	0.017	0.012	a5 V	1.24	1102.0
4	00:56:46.94	+61:10:13.2	13.316	2.974	2.245	1.543	0.693	0.270	0.635	0.012	0.020	0.025	0.015	0.013	0.016	0.012	f5 III	1.023	1056.0
5	00:56:47.02	+61:07:52.1	14.418	3.063	2.268	1.535	0.757	0.260	0.637	0.013	0.021	0.026	0.016	0.016	0.018	0.013	f3 V	1.439	2988.0
6	00:56:47.65	+61:12:25.0	14.963	3.237	2.407	1.661	0.831	0.292	0.685	0.014	0.022	0.026	0.017	0.019	0.021	0.014	f3 V	1.747	3160.0
7	00:56:49.29	+61:03:27.8	13.958	2.780	2.236	1.560	0.649	0.250	0.645	0.013	0.021	0.026	0.016	0.015	0.017	0.013	g1 V	0.445	512.0
8	00:56:51.92	+61:04:50.5	13.377	2.715	2.030	1.309	0.560	0.216	0.506	0.012	0.020	0.025	0.015	0.013	0.016	0.012	f0 V	0.953	849.0
9	00:56:52.75	+61:06:28.4	16.065	3.483	2.919	2.021	0.811	0.357	0.766	0.022	0.036	0.035	0.024	0.012	0.024	0.022	k0 V	0.724	970.0
10	00:56:54.04	+61:09:04.2	17.671	—	3.215	2.039	0.963	0.358	0.740	0.013	—	0.083	0.019	0.014	0.017	0.014	a4 V	3.041	3203.0

(This table is available in its entirety in machine-readable form.)

Table 2
Results of Photometry and Classification of Stars in the Vilnius System for the IC 63 Stars with the Vatican Advanced Technology Telescope (VATT)

No.	R.A. (J2000) (hh:mm:ss)	Decl. (J2000) (dd:mm:ss)	V (mag)	$U-V$ (mag)	$P-V$ (mag)	$X-V$ (mag)	$Y-V$ (mag)	$Z-V$ (mag)	$V-S$ (mag)	$e(V)$ (mag)	$e(U-V)$ (mag)	$e(P-V)$ (mag)	$e(X-V)$ (mag)	$e(Y-V)$ (mag)	$e(Z-V)$, (mag)	$e(V-S)$ (mag)	Sp type	A_V (mag)	d (pc)
1	00:58:39.02	+60:55:56.4	17.717	3.672	—	2.093	0.979	0.375	0.884	0.014	0.063	—	0.020	0.015	0.018	0.016	g1 IV	1.801	3705.0
2	00:58:40.22	+60:52:19.8	14.451	3.211	2.390	1.438	0.649	0.233	0.572	0.013	0.022	0.025	0.016	0.016	0.018	0.012	a2 V	1.847	1265.0
3	00:58:40.73	+60:58:59.0	15.417	3.402	2.561	1.675	0.766	0.284	0.675	0.016	0.027	0.025	0.019	0.024	0.026	0.016	a7 IV	2.051	2416.0
4	00:58:40.94	+60:56:56.2	14.642	6.149	5.142	3.623	1.515	0.585	1.357	0.013	0.030	0.033	0.021	0.022	0.021	0.013	k3 III	2.508	2606.0
5	00:58:41.21	+60:57:08.2	14.825	2.795	2.190	1.551	0.667	0.260	0.631	0.014	0.022	0.025	0.017	0.018	0.020	0.014	f8 V	0.678	948.0
6	00:58:41.25	+60:51:00.1	15.884	4.997	—	2.996	1.236	0.472	1.187	0.012	0.050	—	0.016	0.012	0.015	0.012	k2 III	1.568	5994.0
7	00:58:41.50	+60:54:37.9	16.802	3.730	—	2.114	0.972	0.366	0.901	0.012	0.026	—	0.016	0.013	0.016	0.013	g1 IV	1.772	2533.0
8	00:58:41.88	+60:52:41.7	13.558	2.919	2.127	1.184	0.502	0.188	0.436	0.012	0.020	0.025	0.015	0.013	0.015	0.012	a4 V	1.123	1118.0
9	00:58:42.46	+61:00:33.8	17.253	3.584	—	2.145	0.949	0.345	0.901	0.013	0.038	—	0.017	0.013	0.016	0.013	g6 V	1.489	1499.0
10	00:58:43.51	+60:57:06.2	17.187	3.866	—	1.775	0.813	0.320	0.650	0.014	0.036	—	0.017	0.014	0.017	0.018	a6 IV	2.309	4564.0

(This table is available in its entirety in machine-readable form.)

Table 3
Results of Photometry and Classification of Stars in the Vilnius System for the IC 59 and IC 63 Stars with the Maksutov-type Telescope

No.	R.A. (J2000) (hh:mm:ss)	Decl.(J2000) (dd:mm:ss)	V (mag)	$U-V$ (mag)	$P-V$ (mag)	$X-V$ (mag)	$Y-V$ (mag)	$Z-V$ (mag)	$V-S$ (mag)	$e(V)$ (mag)	$e(U-V)$ (mag)	$e(P-V)$ (mag)	$e(X-V)$ (mag)	$e(Y-V)$ (mag)	$e(Z-V)$, (mag)	$e(V-S)$ (mag)	Sp type	A_V (mag)	d (pc)
1	00:56:15.50	+61:20:35.5	14.864	—	2.899	2.103	1.063	0.407	0.849	0.071	—	0.118	0.100	0.113	0.110	0.118	f5 III	2.563	1405.0
2	00:56:19.17	+61:06:30.2	13.715	2.885	2.292	1.604	0.686	0.291	0.630	0.028	0.060	0.052	0.044	0.035	0.034	0.036	g0 IV	0.636	908.0
3	00:56:19.37	+61:16:50.7	12.919	2.701	2.077	1.396	0.605	0.249	0.591	0.026	0.048	0.041	0.033	0.031	0.029	0.031	f6 IV	0.545	767.0
4	00:56:20.86	+61:11:13.6	14.953	—	2.503	1.751	0.769	0.315	0.700	0.035	—	0.079	0.052	0.044	0.048	0.045	g5 V	0.765	811.0
5	00:56:22.21	+61:04:37.2	14.292	—	3.096	1.973	0.953	0.348	0.875	0.033	—	0.065	0.047	0.042	0.042	0.040	a3 III	3.087	2434.0
6	00:56:22.45	+61:20:29.4	11.068	—	—	1.867	0.910	0.379	0.852	0.068	—	—	0.086	0.088	0.082	0.091	a1 III	0.562	1048.0
7	00:56:22.61	+61:00:17.1	15.062	—	2.406	1.663	0.705	0.305	0.663	0.045	—	0.093	0.058	0.056	0.059	0.069	g6 V	0.474	971.0
8	00:56:25.92	+61:07:08.3	11.934	2.725	2.207	1.515	0.695	0.299	0.510	0.054	0.070	0.068	0.067	0.067	0.078	0.071	g1 IV	0.62	398.0
9	00:56:26.03	+60:51:37.0	14.234	3.219	2.341	1.443	0.724	0.258	0.612	0.030	0.082	0.053	0.041	0.038	0.040	0.040	a0 V	2.28	2056.0
10	00:56:26.69	+61:12:14.2	12.438	2.963	2.153	1.326	0.564	0.239	0.519	0.024	0.047	0.036	0.030	0.029	0.027	0.031	a8 III	1.136	1026.0

(This table is available in its entirety in machine-readable form.)

combined with spectral classifications and photometry from the literature (Wright et al. 2003; Høg et al. 2000) to investigate the quantitative relationship between the observed polarization efficiency (P/A_V) and the radiation field strength, as well as the strength of magnetic fields. In the present work, we perform a similar investigation of the two nearby (at $d \approx 200$ pc) nebulae IC 59 and IC 63 and compare them with LB results of Medan & Andersson (2019).

IC 59 and IC 63 are two reflection and emission nebulae in the Sh 2-185 H II region (at $d \approx 200$ pc) illuminated by the B0 IV star γ Cas (Karr et al. 2005) at a projected distance of $\sim$1.3 pc (IC 63) and 1.5 pc (IC 59) from the nebulae (Andersson et al. 2013; M. Caputo et al. 2021, in preparation). Sh 2-185 is an H II region with a shell of dust with center at γ Cas. IC 59 and IC 63 are two nebulae in this region and remain part of this shell.

We have acquired seven-band photometry in the Vilnius system of the region, which yields both the classification and the visual extinction of the stars probed. We analyze these data together with existing polarization data from Soam et al. (2017) and compare the results to those from the study of the LB (Medan & Andersson 2019).

This paper is organized as follows: The polarimetric and photometric observations are presented in Section 2. Section 3 includes the results of observations acquired for this work. Our results are analyzed and discussed in Section 4, and we summarize our findings in Section 5.

2. Data Acquisition

2.1. Polarimetry

2.1.1. Archival Data

Optical imaging (R-band) polarization measurements of nebulae IC 59 and IC 63 were also extracted from Soam et al. (2017). These observations were acquired with the Aries Imaging Polarimeter (AIMPOL) mounted in the Cassegrain focus of the 104 cm optical telescope, India. Details of observations and data reduction can be found in Soam et al. (2017).

2.1.2. Observations

We obtained spectropolarimetric observations from the Intermediate dispersion Spectrograph and Imaging System (ISIS) in the $\sim f/11$ Cassegrain focus of the 4.2 m William Herschel Telescope (WHT) in the Canary Islands, Spain. These observations were carried out on 2013 October 18 and 19, as part of the proposal C9-WHT4/13B. Both the red and blue sides were used for acquiring data. We used the EEV12 CCD, which provides good quantum efficiency down to the atmospheric cutoff and the R300B grating centered at 0.4 μm. The red+ CCD and the R158R grating centered at 0.64 μm were used for the red arm. We are not discussing blue observations here, as those were corrupted by scattered light. The red observations have a coverage of $\lambda \approx 0.48$–0.95 μm. We extracted the polarization values at 0.65 μm for comparison with archival data. HD 212311 and HD 204827 were used as zero-polarization and high-polarization standards, respectively. The total integration time was divided into eight positions of half-wave plate (HWP) settings for minimizing the influence of systematic errors. The standard IRAF routines were used to reduce the data and extract flux. The ordinary (O) and extraordinary (E) spectra were averaged, for each HWP setting observation, into 0.05 μm bins, and the polarization was calculated by fitting $(E-O)/(E+O)$ to a cosine function (Vaillancourt et al. 2020):

$$\frac{E-O}{E+O} = a + P * \cos 4(\alpha - \theta), \quad (1)$$

where P is the amount of polarization, α is the HWP position angle, and 2θ is the position angle of measured polarization. The factor a indicates the gain differences between O- and E-beams. We calculated the normalized Stokes parameters $q(=Q/I = P\cos 4(\theta))$ and $u(=U/I = P \sin 4(\theta))$. The value of I is the total intensity Stokes parameter. The values of P and θ are calculated as

$$P = \frac{1}{I}\sqrt{Q^2 + U^2} \quad (2)$$

and

$$\theta = 0.5 \arctan\left(\frac{U}{Q}\right). \quad (3)$$

2.2. Photometry

CCD observations in the Vilnius seven-color photometric system of two $13' \times 13'$ areas, centered on the nebulae IC 59 and IC 63, were obtained with the 1.8 m VATT telescope on Mt. Graham, Arizona, using the STA0500A camera and a $4k \times 4k$ CCD chip. Since the areas had no standards of the Vilnius system, tie-in observations to the open cluster IC 1805 were done. This cluster has Vilnius photometry published by Straižys et al. (2013). The angular distance between the IC 59 and IC 63 nebulae and the cluster is about 12°. Processing of CCD frames has been done with the IRAF program package in the aperture mode. The results of photometry of stars down to $V \approx 19$ mag are given in Table 1 (IC 59, 124 stars; online) and Table 2 (IC 63, 185 stars; online). In these tables the last column gives the spectral and luminosity classes in the MK system determined from the photometric data with the QCOMPAR code as described in Straižys et al. (2019). The uncertainties of V magnitudes and color indices U–V, P–V, X–V, Y–V, Z–V, and V–S given in Tables 1 and 2 take into account the measurement errors and the errors of transformation to the standard system.

To cover all the stars with the available polarization data, another set of CCD exposures with a $35' \times 35'$ field of view were obtained with the Maksutov-type 35/50 cm telescope of the Molėtai Observatory in Lithuania, using an Apogee Alta U-47 CCD camera. A field center was selected in between the IC 59 and IC 63 nebulae at R.A.(2000) = 00:58:30, decl. (2000) = +61:01:30. As in the case of the VATT observations, a tie-in to the IC 1805 cluster standards was applied. The processing of CCD frames and the classification of stars have been done with the same methods as in the case of the VATT observations, but the limiting magnitude of Molėtai observations is close to $V = 17$ mag. The catalog of 487 stars, measured and classified from the Molėtai exposures, is given in Table 3 (online).

The values A_V of the measured stars were determined from their color excesses E_{Y-V}, which are the differences between the observed and the intrinsic color indices $(Y-V)_0$ taken

from Straižys (1992):

$$E_{Y-V} = (Y - V)_{\rm obs} - (Y - V)_0, \quad (4)$$

$$A_V = 4.16\, E_{Y-V}, \quad (5)$$

where the coefficient 4.16 corresponds to the normal extinction law. Typical uncertainties of A_V due to the observational errors of Y–V and the errors of the intrinsic $(Y - V)_0$ are ~ 0.1 mag for the stars with $V < 17$ mag and ~ 0.2 mag for the stars with V between 17 and 19 mag.

3. Results

Table 4 presents the stars common in polarization measurements of Soam et al. (2017) and photometry observations toward IC 59 and IC 63. This table shows columns with the coordinates of stars, polarization values, visual magnitude, extinction, and polarization efficiency values (note that we will use the expression "polarization efficiency" to denote the observed line-of-sight-averaged ratio of polarization and extinction (P/A_V)).

Figure 1 shows the map of the degree of polarization measured toward the IC 59 and IC 63 nebulae in a color scale. The structures of the clouds are shown with gray solid curves based on the dust continuum emission of these clouds seen in WISE 12 μm (inset in the upper left corner). The location of the ionizing star and the projected directions of the radiation from γ Cas are also shown. A study by M. Caputo et al. (2021, in preparation) based on [CII] kinematics found that γ Cas lies behind the IC 63 nebula. Therefore, the stars lying outside of IC 63 in the plane of the sky toward γ Cas are not necessarily significantly close to the γ Cas.

Figure 2, adopted from Soam et al. (2017), shows the distribution of the amounts of polarization and the position angles in different regions (marked) toward IC 59 and IC 63 clouds. This figure will be discussed in further sections.

The two panels in Figure 3 show the A_V (top) and P/A_V (bottom) maps toward the IC 59 and IC 63 nebulae. These A_V and P/A_V values are taken from Table 4 for 78 stars in IC 59 and 126 stars in IC 63, respectively. Interstellar extinctions A_V determined from photometry in the Vilnius system are taken from Table 4. These data are plotted in sky coordinates, with their color indicating the magnitude and %/magnitude values, as seen in the color bars, for A_V and P/A_V, respectively. The WISE 12 μm contours in gray color with levels from ~45% to ~60% of the maximum value are plotted to show the dust structure of the nebulae. The location of γ Cas is shown as a black star, and the black arrows mark the direction of radiation from this star to the two nebulae.

The top panel of Figure 4 shows the distribution of extinction values versus their distances from Gaia DR2 (Bailer-Jones et al. 2018). The figure shows an increase in A_V with distances, and this distribution becomes more dispersed beyond 1.2 kpc. The distributions of degree of polarization and position angles with distances of the targets are shown in the middle and bottom panels of this figure. We limited our analysis to stars with distances of less than 1.5 kpc. The explanation for this choice is given in Section 4.1.

Figure 5 shows a toy model/cartoon illustrating the relationship between A_V and distance in the nebulae. This figure is discussed more in Section 4.1 for understanding the variations of extinction values with distances of the projected targets on nebulae IC 59 and IC 63.

Figure 6 is reproduced from the original figure adopted from Lallement et al. (2014). More about this figure is given in Section 4.1.

Figure 7 shows the average results of CO ($J = 1$–0) on-the-fly (OTF)[8] observations toward IC 63 (A. Soam et al. 2021, in preparation). The most prominent emission lines are seen at radial velocities of –20 and 0 km s^{-1}.

Figure 8 shows the polarization efficiency (i.e., P/A_V) values for background stars with measured extinctions in the directions of the IC 59 and IC 63 nebulae. The best-fitting lines to the distributions are also plotted along with equations containing the best-fit parameters in each plot. For plotting these distributions, we have considered only those targets that are at or less than 1.5 kpc away.

The polarization efficiency (P_V/A_V) variation with extinctions for LDN 204- Cloud 3 is shown in Figure 9 by using archival data from Cashman & Clemens (2014).

Figure 10 shows the distribution of polarization efficiencies as a function of radiation flux from the illuminating sources. This plot presents a comparison of the LB with UV flux from OB associations (Medan & Andersson 2019), with our findings toward IC 59 and IC 63 nebulae affected by the UV flux from γ Cas. We also plotted values for LDN 204 adopted from Cashman & Clemens (2014).

A cartoon shown in Figure 11 is adopted from Medan & Andersson (2019) to illustrate the inclination angle (ψ) between the line-of-sight vector and the cloud region.

4. Analysis and Discussion

4.1. Polarization Efficiency and Extinction at Different Distances

To understand the effect of illumination on the grain alignment, we must isolate the dust in, and therefore polarization from, the IC 59 and IC 63 nebula from possible background polarization. We can do this based on the extinction versus distance plots. There are two, likely complementary, origins of steps in these plots (Figure 4). If the surface density (i.e., localized A_V) of each individual extinction layer is uniform, then each step in A_V versus d represents a new layer of dust extinction at the distance of the step. However, multiple steps in A_V versus d can also occur with a single physical, but nonuniform, layer.

We can see this by considering a uniform, but relatively sparse, space distribution of background stars above a given apparent magnitude (i.e., such that they are included in a magnitude-limited photometric survey). The surface density on the sky of observed stars will be the product of their space density and the distance to which the observations extend. The surface density of measured stars will then rise linearly with distance probed, or equivalently, the on-the-sky distance between observed stars will shrink with increasing line-of-sight distance sampled.

If an extinction layer has density enhancements that are small on the scale of the total area surveyed (and, again, the stellar surface density is limited), the probability that such a dense subregion (Figure 5) intercepts the line of sight to a background star will then be significantly less than 1. If the

[8] In this mode of observations, data are acquired with telescope pointing moves between two points on the sky. The telescope slews in the given stripe duration at a constant speed linearly in R.A. and linearly in decl. The OTF mode is typically used to cover large sky areas in short time.

Table 4
Polarization and Extinction Measurements toward IC 59 and IC 63

No.	R.A. (J2000) (hh:mm:ss)	Decl. (J2000) (dd:mm:ss)	$P \pm \sigma_P$ (%)	$\theta_{\rm pos} \pm \sigma_{\theta_{\rm pos}}$ ($^\circ$)	$V_{\rm mag}$ (mag)	A_V (mag)	d (pc)	P/A_V (%/mag)
				IC59				
1	00:56:38.76	+61:12:48.3	1.9 ± 0.5	94.686 ± 7.840	15.831	2.205	2170	0.838
2	00:56:46.94	+61:10:13.2	2.5 ± 0.2	100.928 ± 2.535	13.316	1.023	1056	2.487
3	00:56:47.02	+61:07:52.1	3.1 ± 0.3	65.293 ± 3.649	14.418	1.439	2988	2.124
4	00:56:47.65	+61:12:25.0	1.1 ± 0.1	49.301 ± 3.723	14.963	1.747	3160	0.657
5	00:56:54.04	+61:09:04.2	5.7 ± 1.1	90.927 ± 5.863	17.671	3.041	3203	1.882
6	00:56:56.85	+61:06:41.4	1.7 ± 0.5	58.167 ± 9.562	16.817	2.026	3523	0.816
7	00:56:57.76	+61:14:25.7	1.9 ± 0.7	94.518 ± 11.255	15.955	0.379	1012	4.916
8	00:56:59.27	+61:09:10.9	2.1 ± 0.3	103.422 ± 4.012	13.558	1.069	834	1.984
9	00:57:02.71	+61:06:37.1	2.3 ± 0.1	86.456 ± 1.307	12.692	0.882	1013	2.643
10	00:57:04.70	+61:06:35.9	1.2 ± 0.1	72.787 ± 4.012	14.182	2.800	3944	0.417
11	00:57:05.20	+61:12:50.7	1.2 ± 0.1	90.791 ± 2.586	14.063	0.520	738	2.294
12	00:57:06.74	+61:06:19.5	1.6 ± 0.0	86.517 ± 1.622	12.733	0.616	771	2.568
13	00:57:07.01	+61:10:24.1	2.1 ± 0.1	99.847 ± 1.809	15.242	2.704	2693	0.774
14	00:57:07.11	+61:14:39.6	2.9 ± 0.1	91.215 ± 1.202	14.122	2.184	2338	1.310
15	00:57:07.71	+61:12:34.9	2.2 ± 0.3	95.468 ± 4.670	16.820	1.939	2648	1.115
16	00:57:08.89	+61:14:29.9	2.6 ± 0.3	88.007 ± 3.428	16.169	2.126	2974	1.200
17	00:57:09.45	+61:09:04.3	2.1 ± 0.5	108.411 ± 6.491	17.060	2.658	1348	0.804
18	00:57:10.54	+61:14:38.2	3.6 ± 0.2	92.992 ± 2.247	15.127	1.914	1503	1.858
19	00:57:11.03	+61:04:58.5	2.1 ± 0.7	121.211 ± 9.915	16.972	2.459	2345	0.870
20	00:57:12.35	+61:11:58.8	2.0 ± 0.3	89.814 ± 4.136	16.254	0.803	949	2.487
21	00:57:12.93	+61:14:04.5	2.3 ± 0.2	97.939 ± 2.736	15.730	2.300	1471	1.016
22	00:57:14.96	+61:09:32.2	2.5 ± 0.4	89.062 ± 4.600	15.323	1.107	1028	2.261
23	00:57:17.96	+61:11:31.9	0.8 ± 0.1	79.834 ± 3.958	14.460	2.292	1580	0.361
24	00:57:18.88	+61:08:08.9	3.5 ± 0.7	80.212 ± 6.458	16.440	3.041	2500	1.152
25	00:57:23.69	+61:11:33.5	1.5 ± 0.3	79.678 ± 5.516	14.751	0.957	876	1.596
26	00:57:25.66	+61:12:23.8	2.4 ± 0.1	90.876 ± 1.485	15.110	1.731	2675	1.369
27	00:57:27.73	+61:10:06.6	1.7 ± 0.3	91.326 ± 5.456	15.259	0.990	887	1.729
28	00:57:27.82	+61:12:40.5	1.8 ± 0.2	92.756 ± 3.881	15.473	0.853	1072	2.135
29	00:57:28.33	+61:07:26.5	2.0 ± 0.3	108.154 ± 4.743	15.431	0.820	735	2.493
30	00:57:28.37	+61:09:55.1	2.3 ± 0.3	89.787 ± 3.689	15.715	0.915	1121	2.468
31	00:57:28.42	+61:08:19.1	3.3 ± 0.8	98.010 ± 7.558	17.133	2.271	3862	1.444
32	00:57:30.04	+61:05:01.2	2.1 ± 0.1	83.626 ± 2.078	13.264	1.127	1037	1.846
33	00:57:30.66	+61:11:45.5	1.5 ± 0.2	104.305 ± 5.018	16.059	1.065	718	1.382
34	00:57:32.10	+61:03:14.5	1.2 ± 0.5	86.038 ± 12.259	16.737	1.090	333	1.103
35	00:57:32.74	+61:13:04.9	0.7 ± 0.1	136.687 ± 6.887	12.747	0.291	199	2.268
36	00:57:36.04	+61:08:51.8	2.2 ± 0.4	98.633 ± 5.271	15.511	1.048	833	2.093
37	00:57:36.61	+61:03:38.2	3.0 ± 0.4	89.812 ± 3.912	15.763	0.828	989	3.651
38	00:57:39.63	+61:03:45.8	3.9 ± 0.8	89.027 ± 6.082	17.327	2.192	2144	1.798
39	00:57:40.09	+61:07:45.2	2.0 ± 0.3	109.271 ± 4.617	14.780	1.240	682	1.605
40	00:57:40.36	+61:13:33.0	2.0 ± 0.4	86.359 ± 5.853	16.358	0.807	909	2.523
41	00:57:41.12	+61:04:29.6	3.9 ± 0.4	91.308 ± 3.092	15.937	1.997	1736	1.967
42	00:57:43.20	+61:12:40.2	3.3 ± 0.6	96.742 ± 5.540	16.523	1.597	2592	2.041
43	00:57:47.29	+61:04:46.9	2.4 ± 0.6	84.773 ± 7.809	16.388	1.756	4087	1.370
44	00:57:47.86	+61:14:12.4	1.8 ± 0.3	97.067 ± 5.351	14.050	0.790	910	2.300
45	00:57:49.65	+61:05:58.2	2.5 ± 1.0	85.049 ± 11.645	17.149	1.764	2417	1.423
46	00:57:49.60	+61:12:09.3	1.7 ± 0.6	85.945 ± 10.674	14.927	2.088	3916	0.794
47	00:57:50.56	+61:11:08.9	1.1 ± 0.2	89.669 ± 5.570	14.468	0.624	481	1.798
48	00:57:54.82	+61:11:16.3	3.2 ± 0.5	82.089 ± 4.720	15.168	2.088	1280	1.541
49	00:57:56.72	+61:05:16.4	4.3 ± 1.3	77.353 ± 8.601	17.414	1.718	3290	2.493
50	00:57:57.34	+61:12:22.2	4.3 ± 1.7	121.027 ± 10.697	17.059	1.468	2698	2.941
51	00:57:57.43	+61:07:36.7	1.7 ± 0.6	91.162 ± 10.653	15.876	0.549	913	3.069
52	00:57:58.76	+61:11:14.8	3.1 ± 0.0	85.642 ± 0.857	12.325	1.756	2331	1.784
53	00:58:01.12	+61:12:20.0	2.3 ± 0.5	86.667 ± 7.094	15.704	1.772	3848	1.286
54	00:58:03.45	+61:05:57.6	2.7 ± 1.2	115.314 ± 12.254	17.582	1.302	4231	2.093
55	00:58:06.96	+61:10:52.7	2.4 ± 0.3	87.118 ± 3.724	15.030	1.805	3326	1.336
56	00:58:08.18	+61:11:23.6	3.2 ± 0.1	89.364 ± 1.210	13.724	1.880	1918	1.687
57	00:58:09.16	+61:11:02.9	3.6 ± 0.2	84.604 ± 1.759	14.009	1.448	2419	2.483
58	00:58:12.66	+61:10:34.6	2.3 ± 0.2	88.378 ± 2.853	14.514	0.616	825	3.763
59	00:56:19.17	+61:06:30.2	0.9 ± 0.1	101.670 ± 3.936	13.715	0.636	908	1.373
60	00:56:25.92	+61:07:08.3	0.7 ± 0.0	63.898 ± 3.256	11.934	0.620	398	1.116
61	00:56:27.43	+61:06:50.4	1.6 ± 0.2	71.352 ± 4.878	14.702	1.635	2198	0.968
62	00:56:30.02	+61:10:38.0	1.0 ± 0.4	90.258 ± 11.973	14.272	0.508	662	1.965

Table 4
(Continued)

No.	R.A. (J2000) (hh:mm:ss)	Decl. (J2000) (dd:mm:ss)	$P \pm \sigma_P$ (%)	$\theta_{\rm pos} \pm \sigma_{\theta_{\rm pos}}$ ($^{\circ}$)	$V_{\rm mag}$ (mag)	A_V (mag)	d (pc)	P/A_V (%/mag)
63	00:56:32.96	+61:08:45.7	1.2 ± 0.1	87.730 ± 3.949	12.740	0.316	411	3.867
64	00:56:35.59	+61:05:22.5	1.9 ± 0.3	85.628 ± 4.649	15.195	0.728	919	2.543
65	00:56:52.05	+61:17:11.1	2.3 ± 0.8	98.123 ± 9.709	15.507	0.566	752	4.127
66	00:56:52.43	+61:16:05.1	1.6 ± 0.6	116.492 ± 11.222	15.007	2.542	4963	0.612
67	00:56:56.95	+61:17:46.6	0.5 ± 0.1	88.971 ± 6.332	13.851	0.491	428	1.010
68	00:56:59.40	+61:12:43.4	1.4 ± 0.4	92.845 ± 9.567	15.218	1.951	1949	0.706
69	00:57:33.71	+61:15:27.0	1.4 ± 0.2	103.902 ± 5.628	14.927	0.508	1054	2.801
70	00:57:41.12	+61:02:29.6	1.5 ± 0.5	82.360 ± 10.152	15.628	0.574	1125	2.512
71	00:57:43.50	+61:16:01.2	3.8 ± 0.4	109.991 ± 3.280	15.966	2.675	3342	1.404
72	00:57:43.90	+61:10:48.6	3.3 ± 0.0	90.422 ± 0.552	12.828	2.887	1377	1.152
73	00:57:47.79	+61:15:35.6	3.6 ± 0.1	95.825 ± 1.039	13.583	1.897	2649	1.871
74	00:57:49.60	+61:14:51.5	2.0 ± 0.5	102.537 ± 7.171	15.213	0.670	1042	2.973
75	00:57:53.16	+61:15:46.7	3.6 ± 0.8	92.577 ± 6.638	15.500	1.905	3981	1.875
76	00:57:58.44	+61:15:18.3	0.9 ± 0.3	111.760 ± 8.952	14.323	0.495	553	1.879
77	00:58:05.05	+61:16:15.3	3.7 ± 0.2	96.867 ± 1.719	14.542	1.880	1919	1.988
78	00:58:11.94	+60:50:39.6	1.0 ± 0.4	107.767 ± 10.727	14.473	0.212	1003	4.821
				IC63				
1	00:58:40.22	+60:52:19.8	3.5 ± 0.3	88.268 ± 2.660	14.451	1.847	1265	1.919
2	00:58:41.25	+60:51:00.1	3.3 ± 0.4	87.728 ± 3.571	15.884	1.568	5994	2.126
3	00:58:41.50	+60:54:37.9	3.2 ± 0.7	87.937 ± 6.559	16.802	1.772	2533	1.812
4	00:58:41.88	+60:52:41.7	2.5 ± 0.2	88.994 ± 2.679	13.558	1.123	1118	2.268
5	00:58:46.39	+60:52:12.0	4.5 ± 0.2	89.716 ± 1.324	14.143	1.772	1329	2.554
6	00:58:48.35	+60:56:00.2	1.5 ± 0.1	87.646 ± 2.605	13.458	0.412	561	3.728
7	00:58:50.13	+60:52:14.2	3.9 ± 0.3	88.258 ± 2.180	15.093	1.826	1840	2.162
8	00:58:51.81	+61:01:02.6	2.1 ± 0.0	87.787 ± 1.262	11.541	0.524	922	4.090
9	00:58:52.86	+60:51:55.8	2.3 ± 0.4	80.266 ± 5.431	16.546	1.327	3899	1.707
10	00:58:52.96	+60:55:34.4	1.1 ± 0.2	87.062 ± 6.957	15.050	0.620	727	1.792
11	00:58:53.33	+61:00:12.2	3.3 ± 0.8	68.122 ± 6.816	16.488	2.167	4402	1.542
12	00:58:54.96	+60:51:58.0	3.6 ± 0.4	92.876 ± 3.560	16.107	1.302	1777	2.798
13	00:58:55.05	+60:52:31.9	2.2 ± 0.1	89.438 ± 1.431	13.046	0.703	747	3.137
14	00:58:55.67	+60:59:53.3	3.1 ± 0.5	88.485 ± 5.437	16.302	1.265	4006	2.417
15	00:58:55.66	+60:52:11.2	3.7 ± 0.1	91.288 ± 1.149	14.183	1.797	2818	2.071
16	00:58:55.75	+61:00:11.4	1.4 ± 0.0	87.251 ± 1.229	11.311	0.678	574	2.074
17	00:58:57.22	+60:53:16.8	2.2 ± 0.4	87.184 ± 6.108	15.518	0.795	905	2.745
18	00:59:00.19	+60:55:04.9	1.6 ± 0.4	63.125 ± 8.169	16.261	1.980	3147	0.792
19	00:59:02.80	+60:55:18.1	2.6 ± 0.3	68.499 ± 4.061	15.433	2.167	3730	1.177
20	00:59:04.21	+60:51:27.9	2.5 ± 0.5	94.355 ± 6.622	15.916	1.518	3915	1.637
21	00:59:04.58	+60:50:59.7	4.2 ± 0.3	100.785 ± 2.664	16.578	1.277	1413	3.266
22	00:59:05.49	+60:59:50.9	3.7 ± 0.4	111.196 ± 3.217	15.591	1.444	3163	2.571
23	00:59:05.68	+60:55:00.0	1.4 ± 0.5	90.84 ± 11.048	15.635	0.653	941	2.106
24	00:59:05.91	+60:58:52.0	1.3 ± 0.1	84.027 ± 2.722	13.030	0.516	563	2.591
25	00:59:06.09	+60:52:08.9	4.6 ± 0.8	88.539 ± 5.036	16.594	1.739	4926	2.629
26	00:59:09.71	+60:51:14.3	3.8 ± 0.4	94.481 ± 3.573	16.760	1.676	4970	2.280
27	00:59:10.24	+60:57:07.1	2.1 ± 0.1	89.030 ± 2.176	13.733	0.703	947	3.014
28	00:59:10.34	+60:55:26.7	3.4 ± 0.5	90.528 ± 4.070	16.199	1.514	2292	2.277
29	00:59:11.15	+60:51:48.2	2.8 ± 0.7	90.734 ± 7.378	16.422	1.489	1007	1.863
30	00:59:13.57	+61:00:33.1	2.2 ± 0.1	76.950 ± 1.825	14.266	2.820	1670	0.785
31	00:59:15.41	+60:51:41.5	4.9 ± 0.9	95.312 ± 5.442	16.870	1.298	2232	3.810
32	00:59:16.98	+60:57:39.3	3.9 ± 0.6	66.999 ± 4.609	17.100	1.860	1838	2.087
33	00:59:17.61	+60:52:02.6	2.6 ± 0.3	85.077 ± 3.322	15.254	0.786	1027	3.352
34	00:59:18.12	+60:58:30.6	1.3 ± 0.1	86.726 ± 2.707	12.585	0.620	615	2.058
35	00:59:18.52	+60:55:34.4	1.5 ± 0.1	61.012 ± 2.860	13.966	0.973	291	1.579
36	00:59:19.44	+60:57:57.5	3.9 ± 0.2	95.696 ± 2.082	15.394	1.468	2241	2.669
37	00:59:20.03	+60:59:09.1	2.5 ± 0.1	89.294 ± 1.125	12.302	1.036	947	2.399
38	00:59:22.61	+60:56:48.2	2.3 ± 0.1	87.893 ± 2.180	14.831	2.209	3682	1.057
39	00:59:25.53	+60:58:55.5	2.5 ± 0.3	92.686 ± 4.044	15.340	0.894	1119	2.834
40	00:59:25.54	+60:55:18.7	2.9 ± 0.6	101.108 ± 6.577	16.844	2.471	2929	1.163
41	00:59:28.96	+60:54:43.0	3.7 ± 0.2	81.605 ± 1.719	15.316	2.205	2699	1.658
42	00:59:28.96	+61:00:03.4	2.5 ± 0.0	92.143 ± 0.759	11.479	1.543	1086	1.601
43	00:59:30.70	+61:00:18.1	3.2 ± 0.1	86.815 ± 0.998	13.377	2.109	2374	1.515
44	00:59:31.23	+60:59:50.5	2.6 ± 0.7	59.021 ± 8.202	16.674	1.980	2034	1.320
45	00:59:32.97	+60:54:56.9	3.9 ± 0.4	84.442 ± 2.925	15.422	2.438	2415	1.611
46	00:59:33.06	+60:58:50.6	3.7 ± 0.7	118.725 ± 5.814	16.806	1.643	3936	2.241

Table 4
(Continued)

No.	R.A. (J2000) (hh:mm:ss)	Decl. (J2000) (dd:mm:ss)	$P \pm \sigma_P$ (%)	$\theta_{\rm pos} \pm \sigma_{\theta_{\rm pos}}$ ($^{\circ}$)	$V_{\rm mag}$ (mag)	A_V (mag)	d (pc)	P/A_V (%/mag)
47	00:59:34.51	+61:00:03.0	2.9 ± 0.7	91.207 ± 6.766	16.016	1.810	2211	1.624
48	00:59:36.12	+60:54:26.0	2.2 ± 0.6	102.096 ± 8.783	16.795	2.188	3199	0.995
49	00:59:36.82	+60:54:16.1	5.5 ± 0.7	102.210 ± 3.953	17.227	1.606	2514	3.432
50	00:59:37.24	+60:52:55.4	3.1 ± 0.4	92.239 ± 4.078	15.775	2.059	2251	1.525
51	00:59:37.43	+60:51:03.5	3.3 ± 0.5	96.491 ± 4.399	15.976	1.493	1730	2.201
52	00:59:39.54	+60:49:54.1	2.0 ± 0.2	96.840 ± 3.484	14.191	0.836	1058	2.283
53	00:59:40.78	+60:52:10.7	4.2 ± 0.6	76.369 ± 4.573	16.646	1.918	3685	2.189
54	00:59:41.16	+60:55:00.6	3.4 ± 0.3	102.655 ± 2.811	15.677	2.592	2963	1.295
55	00:59:41.23	+60:59:29.8	4.4 ± 0.4	87.787 ± 2.808	15.870	1.697	4428	2.567
56	00:59:46.19	+60:50:31.1	1.8 ± 0.3	88.516 ± 5.520	15.186	1.477	474	1.217
57	00:59:46.46	+60:51:43.3	5.9 ± 1.0	78.698 ± 5.124	16.811	1.606	4324	3.692
58	00:59:46.54	+60:54:45.2	2.4 ± 0.1	84.220 ± 2.314	14.001	0.907	874	2.599
59	00:59:47.06	+60:53:11.7	2.8 ± 0.4	103.085 ± 4.276	15.840	1.194	2095	2.316
60	00:59:50.58	+60:52:16.8	2.9 ± 0.1	95.544 ± 1.858	14.464	1.681	2378	1.732
61	00:59:50.79	+60:50:52.1	2.3 ± 0.1	94.562 ± 2.426	13.845	1.344	2672	1.684
62	00:59:52.23	+60:51:30.6	2.0 ± 0.2	99.130 ± 3.736	14.544	1.215	2722	1.686
63	00:59:54.68	+60:55:39.2	2.8 ± 0.7	83.939 ± 7.671	16.288	1.776	4421	1.601
64	00:59:55.26	+60:59:57.8	4.3 ± 1.1	90.962 ± 6.089	16.475	0.724	1021	5.978
65	00:59:56.20	+60:54:31.7	3.1 ± 0.4	92.155 ± 3.995	15.556	1.614	2523	1.909
66	00:59:56.45	+61:00:21.1	4.1 ± 2.0	93.549 ± 11.268	16.425	1.581	4570	2.623
67	00:59:57.51	+60:56:07.0	3.0 ± 0.2	83.536 ± 2.715	14.584	1.697	2662	1.743
68	00:59:57.65	+60:55:32.4	4.7 ± 0.4	83.722 ± 2.712	15.857	1.427	2275	3.302
69	00:59:58.13	+60:54:28.7	2.8 ± 0.3	92.243 ± 3.419	15.192	1.660	3526	1.708
70	01:00:00.29	+60:58:44.0	2.5 ± 0.5	89.902 ± 5.267	16.244	1.939	1444	1.273
71	01:00:00.89	+60:54:44.9	3.3 ± 0.4	90.908 ± 3.547	15.625	1.947	2211	1.700
72	01:00:02.44	+60:50:54.1	2.8 ± 0.4	98.487 ± 4.174	15.478	1.564	2281	1.792
73	01:00:02.58	+60:55:28.5	3.8 ± 0.4	80.216 ± 2.971	15.334	1.552	2532	2.421
74	01:00:06.20	+60:49:54.4	2.9 ± 0.6	95.566 ± 5.931	16.155	1.602	2773	1.848
75	01:00:06.35	+60:52:08.5	2.2 ± 0.1	87.631 ± 1.948	13.427	0.986	1070	2.238
76	01:00:09.81	+60:56:46.0	2.7 ± 0.2	92.090 ± 2.374	14.183	1.614	4209	1.658
77	01:00:13.34	+60:53:24.2	1.7 ± 0.2	78.769 ± 3.900	14.232	0.616	684	2.670
78	01:00:13.37	+60:59:55.1	1.6 ± 0.2	91.158 ± 4.516	15.906	0.691	389	2.385
79	01:00:13.98	+60:51:47.3	2.4 ± 0.6	105.824 ± 8.013	16.362	1.082	1650	2.188
80	01:00:14.21	+60:56:05.5	2.5 ± 0.2	88.042 ± 2.506	15.047	1.331	3868	1.841
81	01:00:14.22	+60:59:43.0	2.6 ± 0.3	80.729 ± 3.555	16.368	1.090	1935	2.428
82	01:00:14.26	+60:58:43.7	4.0 ± 0.4	91.987 ± 2.866	16.713	1.884	2022	2.123
83	01:00:14.60	+60:53:58.0	3.3 ± 0.2	90.165 ± 2.275	14.348	1.360	1637	2.403
84	01:00:15.37	+60:51:29.9	2.6 ± 0.6	91.743 ± 7.104	16.781	0.961	755	2.700
85	01:00:17.32	+60:59:36.0	4.8 ± 0.3	94.843 ± 1.735	14.786	1.302	3137	3.677
86	01:00:18.75	+60:52:27.1	2.2 ± 0.1	87.699 ± 1.723	13.013	0.998	908	2.160
87	01:00:19.45	+60:59:51.0	2.9 ± 0.8	89.099 ± 6.795	15.242	1.419	2682	2.056
88	00:58:14.86	+60:51:49.5	2.0 ± 0.1	87.233 ± 1.692	11.699	0.657	957	3.105
89	00:58:17.68	+60:48:39.4	3.0 ± 0.2	104.245 ± 2.378	13.885	1.810	3494	1.680
90	00:58:20.28	+60:48:47.9	2.0 ± 0.6	102.848 ± 9.080	15.819	0.853	2279	2.342
91	00:58:21.13	+60:52:14.8	1.3 ± 0.3	87.450 ± 8.239	14.923	0.869	656	1.503
92	00:58:34.36	+60:52:58.8	1.8 ± 0.2	92.128 ± 3.490	13.815	1.073	916	1.721
93	00:58:34.40	+60:51:05.5	1.9 ± 0.1	89.602 ± 1.686	12.278	0.628	988	3.091
94	00:58:35.05	+60:49:51.9	3.4 ± 0.4	90.982 ± 4.043	15.146	1.889	1765	1.797
95	00:59:04.01	+61:02:42.3	2.8 ± 0.1	93.770 ± 1.402	13.030	0.803	1012	3.441
96	00:59:13.40	+61:03:28.4	2.4 ± 0.2	89.894 ± 3.440	14.605	1.826	2065	1.317
97	00:59:26.12	+61:02:43.8	3.4 ± 0.4	75.750 ± 3.706	15.398	1.718	2317	1.100
98	00:59:31.44	+61:02:10.0	2.1 ± 0.5	87.491 ± 7.598	15.629	0.711	720	3.013
99	00:59:34.51	+61:01:02.2	2.6 ± 0.5	95.467 ± 5.354	15.726	1.797	3268	1.458
100	00:59:41.51	+61:02:12.0	3.6 ± 0.2	88.405 ± 2.045	14.254	1.743	3088	2.064
101	00:59:42.79	+61:02:59.5	3.9 ± 0.1	87.465 ± 1.279	13.671	1.468	2557	2.689
102	00:59:50.41	+61:02:04.6	1.8 ± 0.3	86.122 ± 3.919	14.575	0.957	891	1.894
103	00:59:56.07	+61:02:44.6	2.8 ± 0.6	95.552 ± 5.500	14.106	2.267	1956	1.240
104	00:59:57.48	+60:50:17.7	2.8 ± 0.1	91.732 ± 1.379	12.993	1.423	232	1.966
105	01:00:01.79	+61:02:22.7	2.6 ± 0.3	87.924 ± 3.624	14.653	0.778	1014	3.279
106	01:00:04.33	+60:55:13.8	2.1 ± 0.0	86.651 ± 1.110	12.021	1.065	1884	1.963
107	01:00:11.44	+61:02:44.4	3.0 ± 0.3	89.279 ± 3.065	13.566	2.163	3135	1.387
108	01:00:15.81	+61:03:19.9	3.5 ± 0.6	88.264 ± 4.025	13.764	2.163	3113	1.616
109	01:00:18.82	+61:03:59.1	4.8 ± 1.1	97.847 ± 5.838	15.553	0.670	758	7.161

Table 4
(Continued)

No.	R.A. (J2000) (hh:mm:ss)	Decl. (J2000) (dd:mm:ss)	$P \pm \sigma_P$ (%)	$\theta_{\rm pos} \pm \sigma_{\theta_{\rm pos}}$ ($^{\circ}$)	$V_{\rm mag}$ (mag)	A_V (mag)	d (pc)	P/A_V (%/mag)
110	01:00:20.57	+60:59:04.8	3.8 ± 0.7	93.701 ± 5.588	16.040	0.978	7654	3.867
111	01:00:26.80	+60:55:08.5	3.5 ± 0.5	90.979 ± 4.398	15.132	1.373	2047	2.569
112	01:00:28.68	+60:58:01.1	3.0 ± 0.3	86.084 ± 2.993	14.903	1.835	2160	1.628
113	01:00:30.23	+60:54:25.3	3.4 ± 0.1	89.823 ± 1.547	13.218	0.924	2359	3.703
114	01:00:31.68	+60:59:32.8	5.2 ± 0.5	94.779 ± 2.816	15.075	0.553	710	9.439
115	01:00:34.72	+60:56:34.3	2.8 ± 0.1	85.776 ± 2.005	13.083	1.206	1541	2.282
116	01:00:38.48	+60:54:47.2	1.3 ± 0.1	81.381 ± 2.138	13.332	0.270	496	4.963
117	01:00:40.70	+60:55:34.8	3.3 ± 0.8	86.175 ± 7.674	15.694	0.811	5521	4.033
118	01:00:41.54	+61:00:24.5	3.5 ± 0.2	96.287 ± 1.602	13.721	1.697	3381	2.052
119	01:00:42.81	+60:59:04.2	2.3 ± 0.2	94.634 ± 2.431	15.357	1.011	1369	2.277
120	01:00:49.06	+60:56:37.4	3.2 ± 0.7	95.649 ± 6.757	15.845	1.847	2262	1.738
121	01:00:54.83	+60:58:16.2	1.9 ± 0.2	90.776 ± 3.49	15.552	1.681	2293	1.136
122	01:00:55.36	+60:58:40.7	2.3 ± 0.2	95.924 ± 2.804	13.318	1.352	2579	1.707
123	01:00:55.35	+60:59:58.5	1.5 ± 0.2	85.505 ± 3.513	14.399	0.270	548	5.737
124	01:00:57.55	+60:58:22.2	2.2 ± 0.2	90.538 ± 2.608	15.401	1.793	2645	1.240
125	01:00:57.81	+60:59:21.5	2.1 ± 0.8	104.854 ± 11.705	16.199	1.664	2402	1.253
126	01:00:58.86	+60:57:28.7	1.0 ± 0.1	86.954 ± 3.087	14.282	0.399	342	2.388

(This table is available in machine-readable form.)

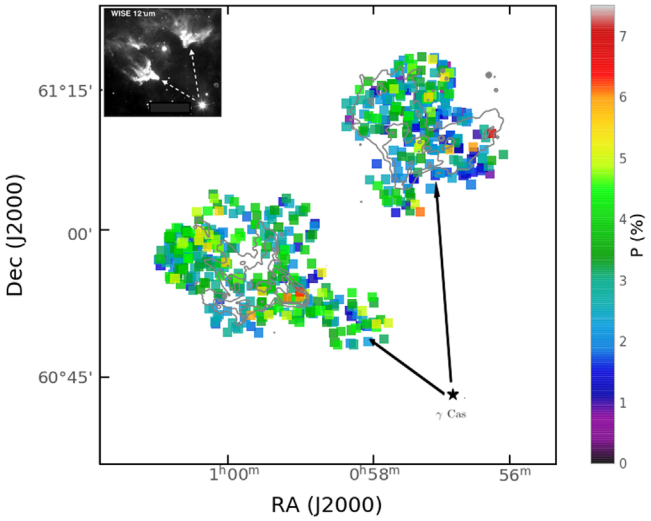

Figure 1. Maps of the amount of polarization observed toward the nebulae IC 59 and IC 63. The inset in the upper left corner shows the WISE 12 μm dust continuum maps of these nebulae. The location of ionizing star γ Cas and the directions of radiation hitting the nebulae are shown with the star symbol and dashed arrows, respectively.

extinction density enhancements have a characteristic scale size, then an "extinction step" will occur at the distance where that scale size is first effectively sampled by the stellar surface density. For a spectrum of extinction enhancement scales, we would expect a more distributed increase in A_V versus d, yielding increased dispersion in extinction for a given stellar distance.

In this scenario of an extended low-extinction layer with embedded localized higher-extinction regions, we would expect the upper envelope of the extinction to rise either abruptly—for a single scale size of denser regions—or gradually for a distribution of high-A_V "clumps." The lower envelope, corresponding to the large-scale low-extinction part of the layer, should, however, stay close to constant. For an additional distinct extinction layer, the lower envelope of the A_V distribution should also rise.

It is, of course, also possible to consider an interstellar density distribution where the dense (higher-A_V) regions of a physical extinction layer are more broadly distributed with smaller, low-A_V "hole" areas interspersed (see Figure 5). This would, however, still raise both the upper and lower envelopes of the A_V distribution at the characteristic distance, with a small number of lower-A_V points remaining, and should still be differentiable from a uniform physical layer or a single inhomogeneous one. This is illustrated in the distributions of A_V versus d panels of Figure 4.

Therefore, the better diagnostic of a true additional extinction layer with distance will be the minimum extinction as a function of the distance, rather than the maximum extinction as a function of the distance. The top panel of Figure 4 illustrates this for the direction of Sh 2-185. As is clear from the figure, while there are enhancements of the maximum extinction toward IC 59 and IC 63 between 700 pc and 1.2 kpc, the lower envelope of the extinction remains approximately constant all the way from ∼200 pc to ∼1.2 kpc. At about 1.2–1.5 kpc a significant increase occurs in both the upper and lower envelopes of the extinction distribution, with a small number of low-extinction points remaining at $A_V \lessapprox 1$ mag.

This interpretation is consistent with the trigonometric parallax distances to γ Cas, on the one hand, and the Perseus arm, on the other. The Hipparcos distance for γ Cas (l, $b = 124$, –2) is 188 ± 20 pc. The distance to the Perseus arm can be estimated from the Gaia distance to the OB stars in the star-forming complex W3 (l, $b = 134$, +1) of ≈2.2 kpc (Navarete et al. 2019). Since the OB stars are expected to be concentrated toward the center of the spiral arm, we could expect the dust in the arm to be detectable somewhat closer than the OB stars. We therefore assume in our subsequent analysis that stars out to 1.5 kpc probe only the extinction from dust in Sh 2-185.

Figure 6, adopted from Lallement et al. (2014), shows the differential opacity in the Galactic plane out to ∼1 kpc. The two overlaid arrows are scaled to represent 1 kpc distance and span the Galactic longitude range of 123.°45–124.°05 (i.e., from just west of IC 59 to just east of IC 63). As the figure shows, the differential opacity in this direction is low out to ∼200 pc,

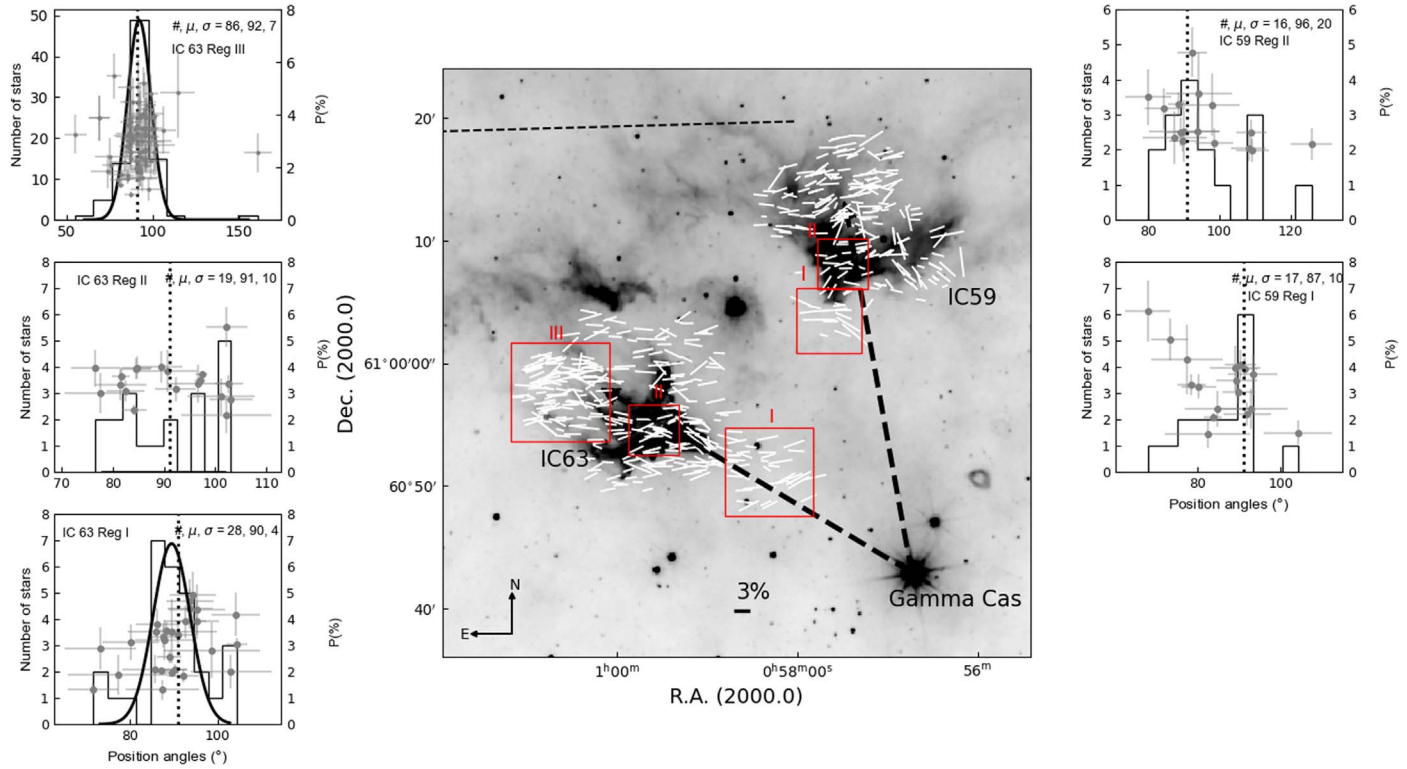

Figure 2. Orientation of the polarization position angles measured for the stars projected toward IC 59 and IC 63 clouds drawn on the 48′ × 48′ WISE 12 μm image. The nebulae, IC 59 and IC 63, and the ionizing star, γ Cas, are identified and labeled. The lengths of the line segments correspond to the measured P. A 3% line segment is drawn for scaling. The arrows with thick dashed lines show the direction of the ionizing radiation. The arrows pass through the densest part of the nebulae identified from the 12 μm intensity. The dashed line shown in the upper left corner represents the inclination of the Galactic plane. The Gaussian fitted histograms with the distribution of P and θ_P corresponding to the regions marked in IC 63 and IC 59 are also shown. This figure is adopted from Soam et al. (2017).

where a high-opacity ridge intercepts our lines of sight (as Figure 3 in Lallement et al. shows, the sampling density of their data indicates that the depth of this ridge is likely, at best, marginally resolved). Beyond this ridge, no further high-opacity material is seen to the extent of the mapping (although beyond ∼700 pc the spatial resolution in the Lallement et al. data decreases, and therefore small-scale structure may not be detected close to the Perseus arm). Thus, our interpretation of our A_V versus distance plots is consistent with the extinction mapping of Lallement et al. (2014).

In addition, we investigated CO ($J = 1$–0) data from Dame et al. (2001) at multiple positions in the near vicinity of IC 59 and IC 63. All positions show a strong CO band with radial velocity close to –20 km s^{-1}. According to the "Kinematic Distance Calculator" (Reid et al. 2009), this velocity gives a distance of the cloud close to 1.5 kpc. This is in agreement with our A_V versus distance plots for the VATT photometric data (top panel of Figure 4), which at about 1.5 kpc show a steep rise of the extinction up to A_V close to 3 mag. It is interesting that the Dame et al. radio data do not show any significant intensity maximum at radial velocity close to zero, which would correspond to the IC 59 and IC 63 clouds at 200 pc. We note that the Dame et al. (2001) surveys are sampled only on a 7′.5 grid and hence the small molecular cores of IC 59 and IC 63 would be significantly beam diluted in their data. However, we found some significant CO ($J = 1$–0) emission at radial velocity close to zero toward IC 59 and IC 63 in our 13 m single-dish observations (A. Soam et al. 2021, in preparation)[9] from Taeduk Radio Astronomy Observatory (TRAO) with much better resolution (44″) than that of observations of Dame et al. (2001). Figure 7 shows the emission at 0 km s^{-1} and close to –20 km s^{-1} radial velocities. Jansen et al. (1994) also reported a detection of CO ($J = 2$–1) in the IC 63 nebula at a radial velocity of 0.6 km s^{-1}. Heyer et al. (1998) found a CO ($J = 1$–0) emission at a velocity close to 0 km s^{-1} located behind the curved surface of IC 59 facing radiation from γ Cas. Our recent observations of CO ($J = 1$–0) and these previous studies show that there is a prominent CO emission toward the IC 59 and IC 63 nebulae. As we discussed above on emission from six positions around these nebulae from Dame et al., the emission seen at –20 km s^{-1} might correspond to the Perseus arm. From these arguments, we conclude that no strong widespread absorbing and polarizing clouds are present behind γ Cas up to 1 or 1.5 kpc.

4.2. Grain Alignment due to External Radiation and Comparison with the LB

Cashman & Clemens (2014) studied the variations of H-band polarization efficiency (P_H/A_V) in the LDN 204-Cloud 3 with distance from ζ Oph (spectral class O9.5 V). They found that the polarization efficiency steadily decreases with the distance from ζ Oph. In addition, the power-law fit to the distribution of polarization efficiency and extinctions shows a steep index of -0.74 ± 0.07, which suggests less grain alignment at high extinctions compared to other studies performed on different molecular clouds. They noticed (beyond the uncertainties) that the weighted mean polarization efficiencies (P_H/A_V) do vary systematically with distance to ζ Oph.

[9] A detailed analysis of line observations is beyond the purpose of this paper and will be presented in a work under progress.

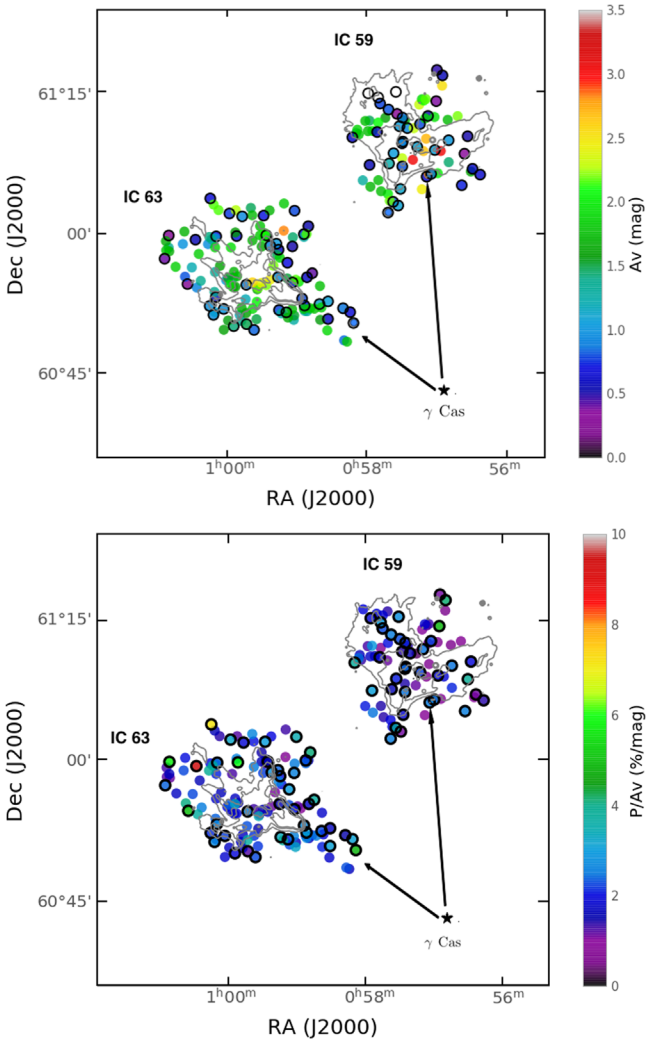

Figure 3. Top panel: map of A_V measurements in IC 59 and IC 63. Gray contours are WISE 12 μm dust emission. Bottom panel: same as the top panel, but for P/A_V values. Symbols with thick boundaries are up to 1.5 kpc and are used in making Figures 4 and 8.

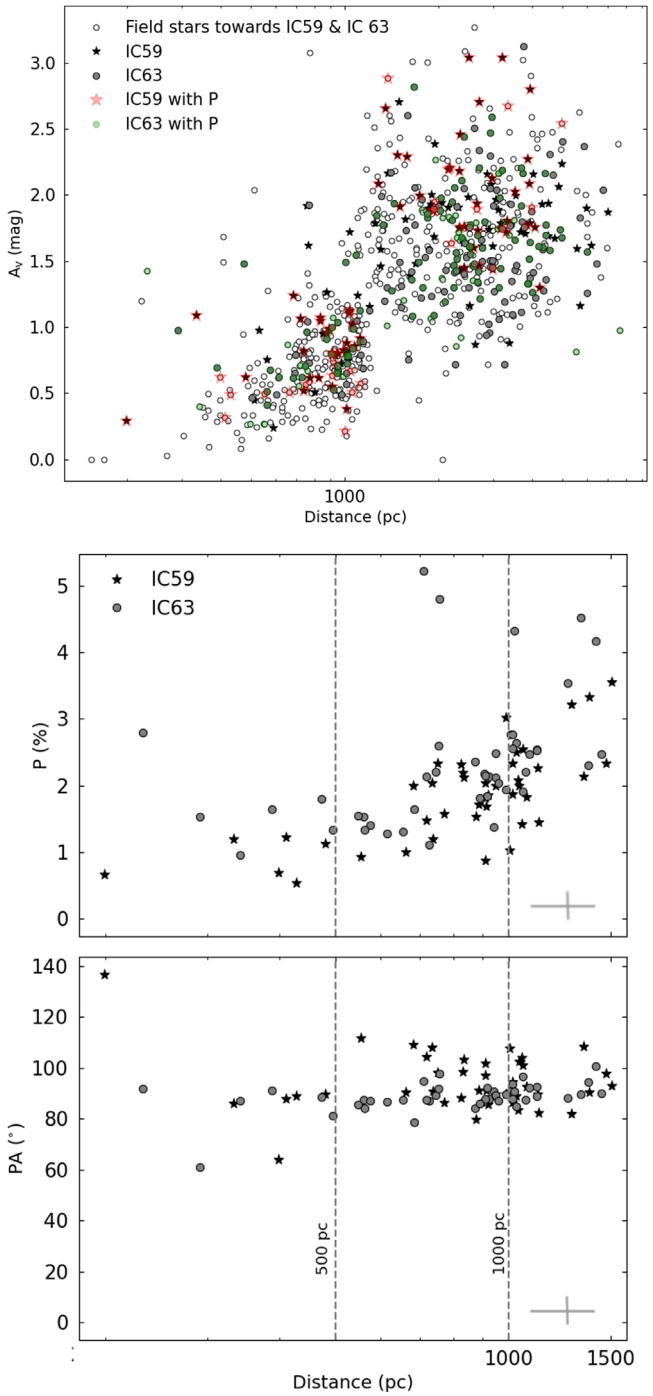

Figure 4. The top panel shows the distribution of A_V values with Gaia DR2 distances from Bailer-Jones et al. (2018) of all the targets where we have photometric information only, and colored symbols are those where we have both photometric and polarimetric data. The two samples of IC 59 and IC 63 are shown with different symbols. The middle and bottom panels show the distributions of the degree of polarization and the position angle with distances. Two vertical dashed lines are drawn at distances of 500 and 1000 pc.

Medan & Andersson (2019) performed a more general study of the grain alignment variation in the LB wall, using a large polarization survey of the north Galactic cap from Berdyugin et al. (2014). They found that the polarization efficiency is linearly dependent on the intensity of the illumination of the grains and is dominated by the light from the OB association within 150 pc. Adding in contributions from field stars also allowed them to investigate the wavelength dependence of RAT alignment and to show that the alignment is most sensitive to the blue light from O- and B-type stars.

In the present study, we add a well-defined system with two nebulae radiated on by higher radiation flux from γ Cas, a B0 IV star, in the Sh 2-185 HII region.

For some regions in Figure 1 no projected star was bright enough to yield significant polarization detections. The spatial distribution of polarization efficiencies shown in the bottom panel of Figure 3 indicates relatively higher polarization efficiencies on the cloud boundaries in low-density regimes. Figure 2, adopted from Soam et al. (2017), shows a similar trend, where the polarization measurements in regions I, II, and III in IC 63 and regions I and II in IC 59 (labeled in red color) show a polarization fraction that is relatively higher in regions closer to γ Cas, especially in IC 59. The polarization efficiency as a function of visual extinction can be interpreted in the framework of Jones et al. (1992):

$$\frac{P}{A_V} = \beta {A_V}^{\alpha}, \quad (6)$$

where α depends primarily on the turbulence of the medium and—for large extinctions—grain alignment variation (Alves

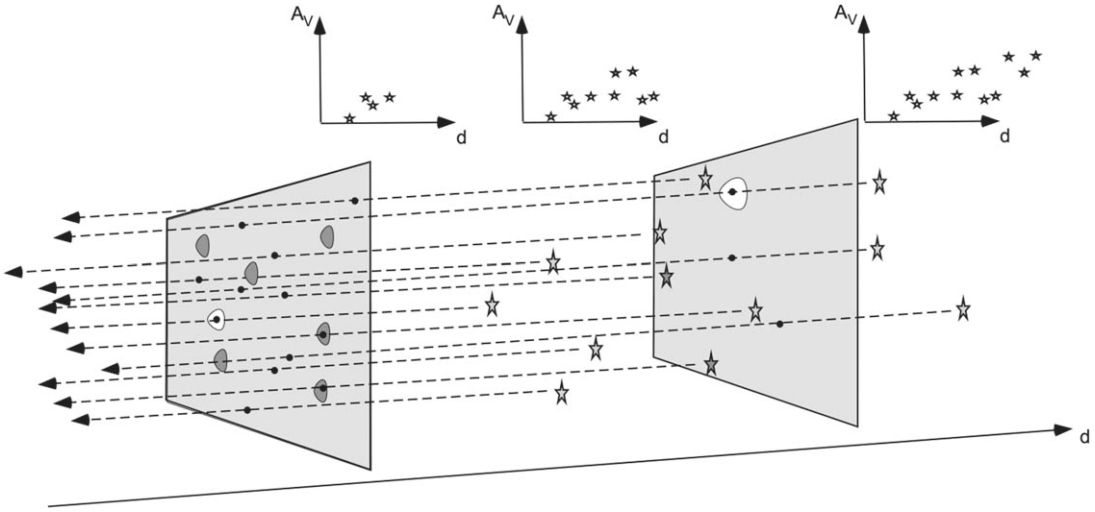

Figure 5. The two causes of extinction steps in an extinction vs. distance plot are illustrated in a toy model/cartoon. For a cloud with a density structure—especially where the surface area of the high-extinction regions is significantly smaller than the average extinction of the cloud/layer—an extinction jump may be detected at a distance corresponding to where the chance of a line of sight encountering a "clump" becomes significant. The lower envelope of the distribution will, however, stay fixed. When a second extinction layer is encountered, both the upper and lower envelopes of the distribution will change. For extinction layers with low-density subregions ("holes" shown as white regions in the screens), a small number of low-A_V outliers may be expected. These different behaviors can all be seen in the top panel of Figure 4.

et al. 2014; Jones et al. 2015). For a fully turbulent medium, α is expected to take a value of –0.5, indicating a random walk through a large number of turbulent cells with differently oriented magnetic fields (Jones et al. 1992). The value at $A_V = 1$ can be used as a comparison of the polarization efficiency between samples. Under the assumption that the inherent dust characteristics (roundness, size distribution, mineralogy, etc.) are similar for the different regions, P/A_V at $A_V = 1$ can be used as a tracer of grain alignment efficiency.

We used Equation (6) to fit the polarization and extinction measurements toward IC 59 and IC 63 shown in Figure 8. We considered data up to 1.5 kpc only for plotting and fitting in this figure. The reason for choosing this distance is given in Section 4.1. We find values of α and β of -0.55 ± 0.09 and 2.35 ± 0.04 for IC 63 and -0.41 ± 0.08 and 1.88 ± 0.04 for IC 59, respectively. As we stated above in Section 2, we used a typical error of 0.1 mag in A_V for calculating uncertainties in fitted values. To evaluate the sensitivity of the results to systematic errors (such as the incorrect assignment of any polarization or extinction to the two clouds), we systematically removed one line of sight from the sample for each cloud and recalculated the power-law fits. The resulting sample of fit parameters are consistent with the fit to the full sample for each cloud, indicating that the fit results are dominated by random errors and that the results are robust. For IC 63 the α parameter distribution has a mean of -0.55 with an error on the mean of 0.03, while the β parameter has a mean of 2.34 with an error on the mean of 0.02. For IC 59 the two distributions have means and error on the means of α:(-0.45,0.03) and β:(1.89,0.07), respectively.

Cashman & Clemens (2014), in their study of Cloud 3 of LDN 204 near ζ Oph, found a slope in P_H/A_V of $\alpha = -0.74 \pm 0.07$. Because of the shape of the Serkowski curve (Serkowski 1973), the near-IR polarization is significantly less than that for optical bands, for almost any extinction. We therefore need to convert the *H*-band data from Cashman & Clemens (2014) to estimated *V*-band polarization, in order to compare their results to the LB wall results. In addition, as suggested by Whittet et al. (2001) and confirmed and expanded on by Andersson & Potter (2007), a universal relationship exists between $\lambda_{\max}$ and A_V, with a secondary dependence on the average ratio of total to selective extinction (R_V) in each region. Because the peak of the polarization curve shifts to longer wavelength with increasing extinction, the transformation from P_H to P_V will depend on the extinction of the line of sight and will result in a steeper P_V/A_V versus A_V relation than for P_H/A_V versus A_V. We used the $\lambda_{\max}$ versus A_V relationship from Andersson & Potter (2007), together with extinction estimates from Cashman & Clemens (2014), to convert the *H*-band measurements to estimates of the V-band polarization and thence derive P_V/A_V values. Performing this conversion from P_H/A_V to P_V/A_V yields an equivalent, *V*-band α value for LDN 204 of $\alpha = -1.24 \pm 0.07$.

Figure 10 shows the variation of polarization efficiency represented by $\beta(\sin\psi)^{-1}$ (assuming $\sin(\psi) = 1$, i.e., $\psi = 90°$, β is equivalent to a lower limit of the alignment efficiency ($P/A_V(A_V = 1)$), Equation (6)) with flux L_*/r^2, where L_* is the luminosity of γ Cas. These expressions are explained later in this section.

As is shown in Figure 10, the values of polarization efficiencies (P/A_V ($A_V = 1$)) are significantly higher in Sh 2-185 than those found in the LB wall with $\beta = 1.95 \pm 0.05$ for IC 59 and $\beta = 2.24 \pm 0.04$ for IC 63. This indicates a higher grain alignment efficiency in the Sh 2-185 region. Similarly to the results by Cashman & Clemens (2014) in the LDN 204 cloud, we also derived a decrease in polarization efficiency for IC 63 and IC 59 with increasing distance from γ Cas. The polarization efficiency in this context refers to $\beta(\sin\psi)^{-1}$, which is inversely proportional to the square of the distance (r) of the cloud from γ Cas. As seen in Figure 10, the $\beta(\sin\psi)^{-1}$ value of IC 59 is less than that of IC 63. This is because IC 63 is relatively closer ($r = 1.3$ pc) to γ Cas than IC 59 ($r = 1.5$ pc). For LDN 204, using the P_V/A_V plot, we derive $\beta = 3.72 \pm 0.04$.

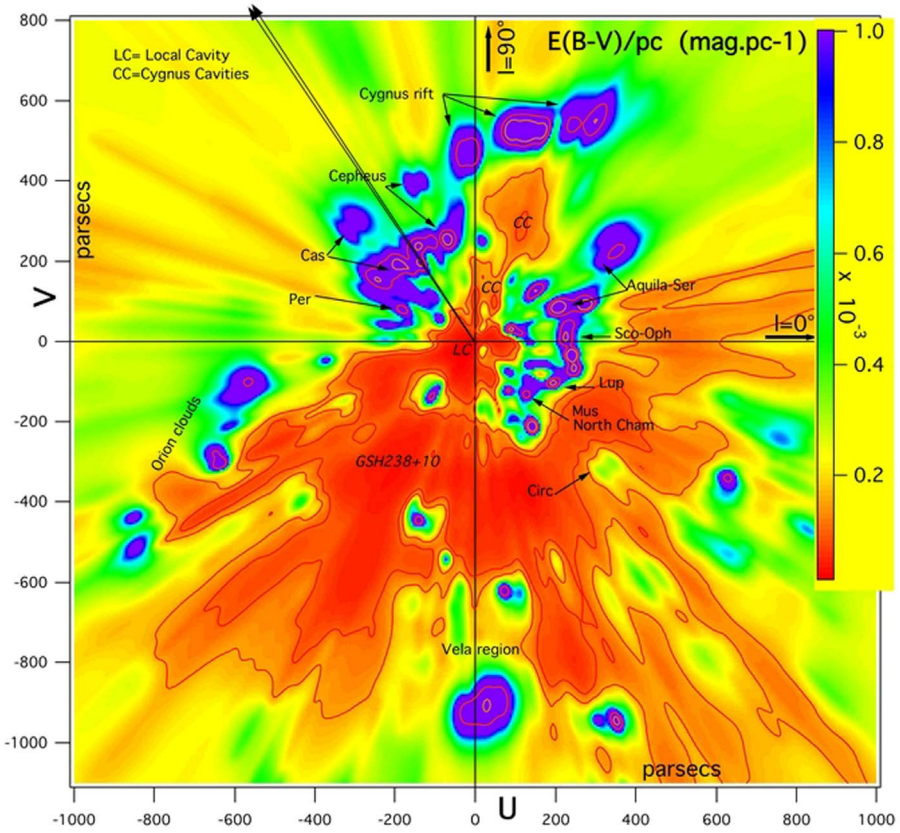

Figure 6. Figure adopted from Lallement et al. (2014) and reproduced with permission © ESO. The inverted differential opacity distribution in the Galactic plane in the solar neighborhood is shown. The Sun is located at (0,0) coordinates with the Galactic center toward the right. The color scale from red to violet shows increasing differential opacities. The two arrows are scaled to be 1 kpc in length and drawn to bracket the extent of the Sh 2–185 region (i.e., from just west of IC 59 to just east of IC 63). The extinction distribution in this map supports our conclusion of very little foreground extinction, or background extinction to at least 1 kpc, in the direction of Sh 2-185.

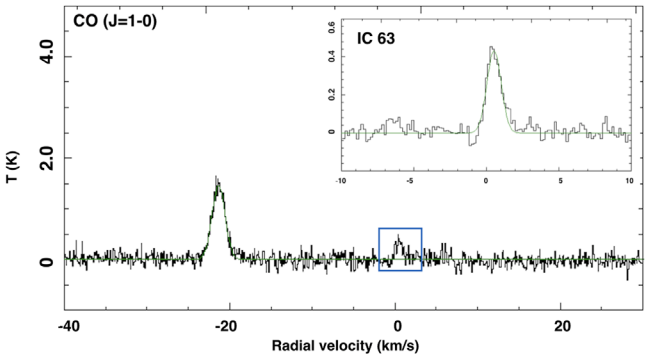

Figure 7. Emission toward IC 63 in the CO ($J = 1$–0) line (Soam et al. 2021, in preparation). The dominant peaks are seen at radial velocities close to –20 and 0 km s^{-1}. A zoom-in of the line feature at 0 km s^{-1} framed with the blue box is shown in the upper right corner of the figure.

To test the variation of radiatively driven grain alignment with distance of the cloud from the radiation sources, Medan & Andersson (2019) constructed a model to predict values of $\beta(\sin\psi)^{-1}$ for the Local Bubble. The model was defined as

$$\beta(\sin\psi)^{-1}(\ell, b) \propto \frac{L_*}{(x_* - x_i)^2 + (y_* - y_i)^2 + (z_* - z_i)^2}, \quad (7)$$

where $L_*^{(i)}$ is luminosity of the source i, x_* (etc.) are the locations of the source, and x_i (etc.) refer to the position at the nebula (wall of LB). Combining all the sources in LB, the model of Medan & Andersson (2019) takes the form

$$\beta(\sin\psi)^{-1} = A + B \cdot \Sigma \frac{L_*^{(i)}}{r_i^2}, \quad (8)$$

where $L_*^{(i)}$ is the luminosity of the source i at a distance r_i from the cloud. The function $\sin\psi$ accounts for the fact that dust-induced polarization only probes the magnetic field component in the plane of the sky. Since the grains are spinning around the field lines, no polarization is generated along the magnetic field direction (see Medan & Andersson 2019, for details). Figure 11 illustrates the concept.

Under the assumption of RAT alignment the alignment efficiency will depend on the intensity of the radiation field at the location of the grain. This will, in turn, depend on the extinction between the illumination source and the grain and, if the radiation field is dominated by a point source, the distance from the source to the grain (through the r^{-2} dependence). For regions with rapidly varying radiation fields (i.e., close to a point source) or with significant extinction, the measured polarization efficiency (P/A_V) may sample regions with different alignment efficiency, especially at higher observational line-of-light visual extinction. However, because of the RAT condition, $\lambda < 2a$, and because the extinction curve falls to the red, RAT alignment is relatively insensitive to the extinction between the source and the grain

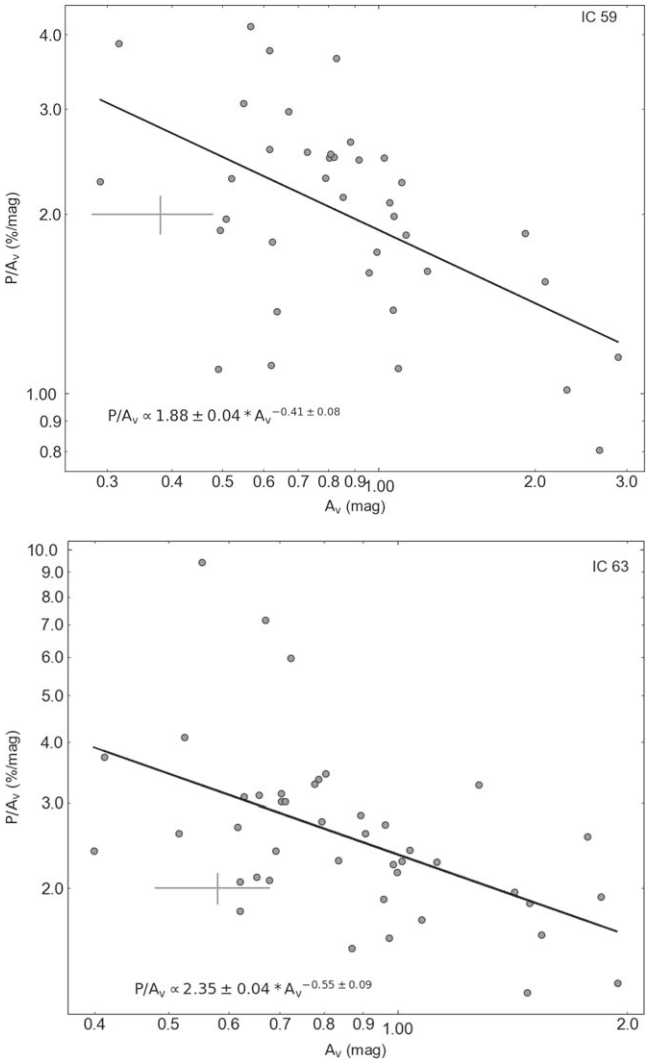

Figure 8. Variation of polarization efficiencies with extinction values measured toward the targets projected on the IC 59 (top) and IC 63 (bottom) nebulae. The best-fitted parameters and typical error bars are also indicated.

for moderate column densities, which will somewhat lessen the variability relative to the visual ($\lambda = 0.55\ \mu$m) extinction. In addition, along an observed line of sight the polarization efficiency will probe dust and gas at varying levels of source-to-grain extinction in a poorly constrained way that depends on the density and location of the cloud relative to the illuminating source. Because the power-law fits in Medan & Andersson (2019) and Figure 8 (this work) are dominated by line-of-sight extinction with $A_V < 1$ mag, internal radiation damping in these clouds should not have a significant impact on the fitted α or β values. In Figure 9, which shows the data from Cashman & Clemens (2014) after transformation from P_H/A_V to P_V/A_V (from their archival data), we used only those detections where $P/\sigma P > 3$ is satisfied. The H-band polarization values are transformed to V-band using the relation from Andersson & Potter (2007); the larger best-fit α value may indicate a significant contribution of cloud-internal extinction vis-à-vis ζ Oph (suppressing the alignment efficiency, and therefore P/A_V, at the higher extinctions). However, as the points at $A_V < 1$ are continuous with the ones at $A_V > 1$, the β value is unlikely to be severely affected,

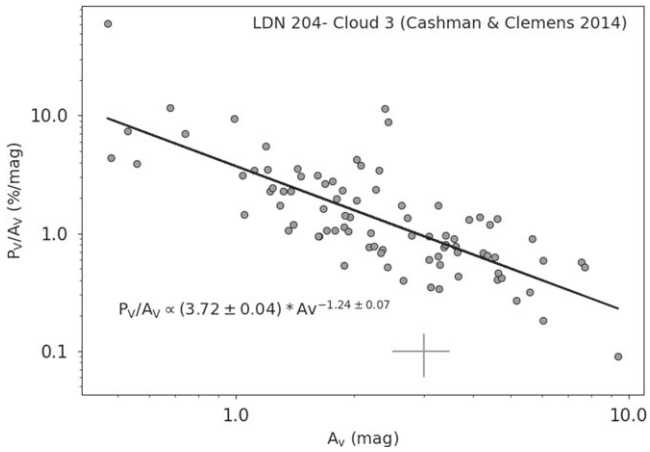

Figure 9. Polarization efficiency (P_V/A_V) vs. extinction distribution of stars observed toward LDN 204-Cloud 3. The data are adopted from Cashman & Clemens (2014). From their archival data, we used only those detections where $P/\sigma P > 3$ is satisfied. The H-band polarization values are transformed to V band using the relation from Andersson & Potter (2007).

certainly not to the level of $\beta \approx 13$ that the straight line of the LB wall and Sh 2-185 results would imply.[10]

For the region between Galactic latitudes 30° and 42°, Medan & Andersson (2019) found $A = 0.0055 \pm 0.0103$ and $B = 0.0047 \pm 0.0002$ from the best fit of model-predicted radiative-driven grain alignment based on luminosities of local OB association versus the measured grain alignment (see Figure 12 of Medan & Andersson 2019).

For IC 63 and IC 59 we assume that the magnetic field is oriented close to the plane of the sky and, therefore, $\sin(\psi)$ is unity. Crutcher et al. (2003) showed that the average Galactic magnetic field in the solar neighborhood is directed toward l, $b \approx 80.6, 0$. Since Sh 2-185 is located at $l \approx 124°$, this means that the Galactic magnetic field, nominally, makes an angle of $\psi \approx 46°$ with the clouds in the region. However, because of the dynamics of a magnetized H II region (Stil et al. 2009; Gendelev & Krumholz 2012), it is not clear that the magnetic field threading IC 59 and IC 63 agrees with the direction of the Galactic average. As shown by the polarization mapping by Soam et al. (2017), a significant plane-of-the-sky component of the magnetic field is present in the nebulae. As noted above, an assumption of $\sin(\psi) = 1$ (i.e., $\psi = 90°$) makes β equivalent to a lower limit of the alignment efficiency ($P/A_V(A_V = 1)$, Equation (6)). Given the distance of the nebulae from γ Cas of 1.3 and 1.5 pc (Hoang et al. 2015), we can put the results for Sh 2-185 on the same plot as those for the LB wall.

Figure 10 shows the values of polarization efficiency modified by $\beta(\sin\psi)^{-1}$ in the LB (Medan & Andersson 2019) with luminosities from of the blue source(s) modified by their distances from the clouds. Overlaid are the resultant values for IC 59 and IC 63 corrected for the Sh 2-185 geometry (M. Caputo et al. 2021, in preparation). As is evident from Figure 2, some of the dust in Sh 2-185 extends beyond the immediate confines of the two clouds. The exact location of this dust is not clear, but given the dynamics of H II regions, it is likely to be either associated with the dense clouds or swept up in an irregular shell around the star. While this means that the exact level of the radiation field strength at the location of this dust is

[10] If we calculate $\beta(\sin\psi)^{-1}$ using best-fitted A and B values of the Local Bubble and IC 59 and IC 63 nebulae and $L/r^2 \approx 3000$ of LDN 204, we get a value close to 13.

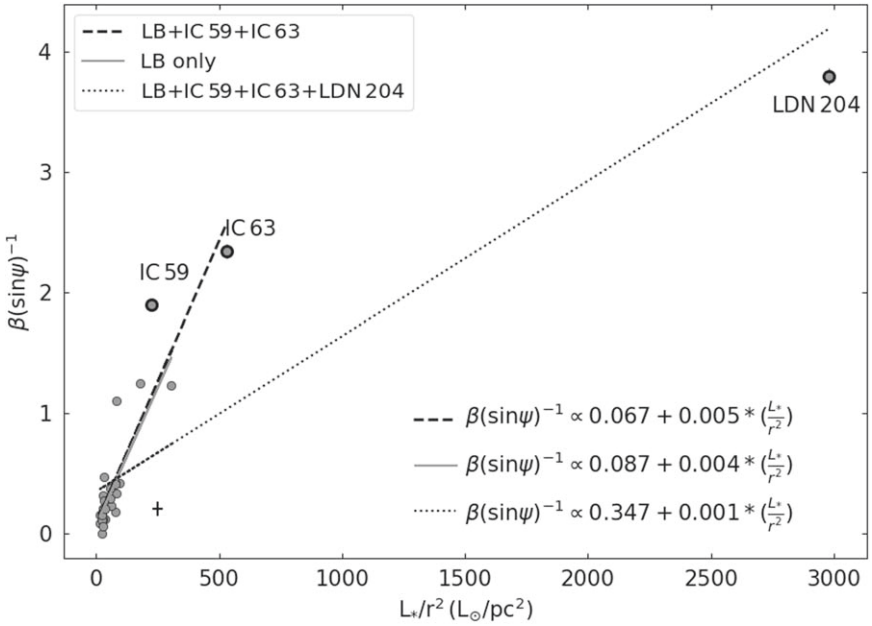

Figure 10. Variation of the polarization efficiency indicated by $\beta(\sin\psi)^{-1}$ (see Medan & Andersson 2019) with UV photon flux. The values measured toward the LB (Medan & Andersson 2019) are shown with gray filled circles, and those of IC 59, IC 63 (this work), and LDN 204 (Cashman & Clemens 2014) with errors are shown as gray filled circles with thick black boundaries. The typical error bar on LB measurements is also shown. The source of UV fluxes toward IC 59 and IC 63 nebulae is γ Cas, and for LDN 204, it is ζ Oph. The walls of LB receive UV flux from OB associations.

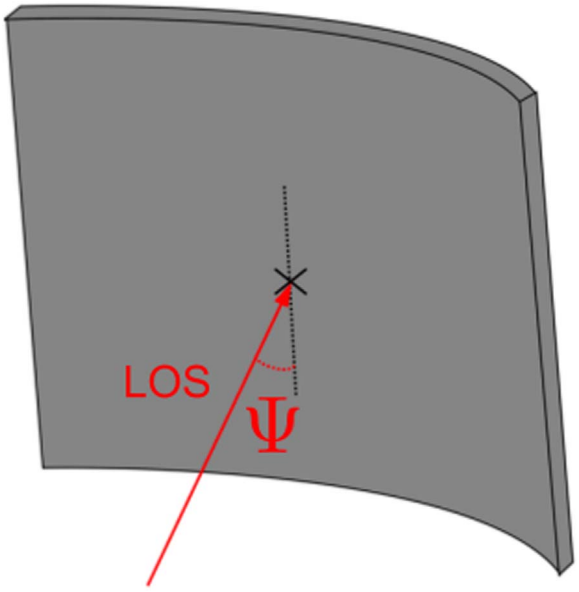

Figure 11. Adapted from Medan & Andersson (2019). The diagram represents one of the regions of the LB wall. The center of the region is intersected by the line-of-sight vector in red color. The inclination angle between the line-of-sight vector and the shaded cloud region is represented by ψ.

also unclear, we assign each of these lines of sight to the nearest of the two clouds and treat the unknown difference in radiation field strength as systematic errors. As discussed above, systematically excluding individual data points from the analysis does not change our results, indicating that these uncertainties do not dominate the behavior of the grain alignment in Sh 2-185. Finally, the alignment efficiency and estimated illumination flux based on the data for LDN 204 from Cashman & Clemens (2014) are also plotted.

As seen in Figure 10, for the LB wall data alone Medan & Andersson (2019) found a best linear fit of $A = 0.067 \pm 0.012$ and $B = 0.0047 \pm 0.0002$. Including the results for IC 59 and IC 63 yields parameter values of $A = 0.087 \pm 0.011$ and $B = 0.0044 \pm 0.0002$, within the 2σ mutual errors of the fits for the LB wall alone. If we include the results for LDN 204-Cloud 3 (Cashman & Clemens 2014), a significantly shallower slope results, but with a poorer fit to the low-luminosity end, with parameters $A = 0.347 \pm 0.023$ and $B = 0.0013 \pm 0.0001$.

Because not all grains can cause polarization (due to sphericity, grain mineralogy, etc.), we would, under RAT alignment, expect that there will exist a radiative illumination intensity where the observed linear relationship between polarization efficiency and radiation intensity breaks down, since at that intensity all grains that *can* be aligned *will* be aligned. It is possible that the change in slope seen when including the LDN 204-Cloud 3 (Cashman & Clemens 2014) results is an indication of such a saturation effect. We are in the process of exploring the polarization efficiency in even more extreme environments where this possibility can be further tested.

4.3. Comparison with Modeled Values

Hoang et al. (2015) analytically modeled the grain alignment by radiative torque in the IC 63 nebula. The presence of external high-energy radiation provides extra torque to the dust grains, providing an opportunity to quantify the RAT and effects of additional torque. Hoang et al. (2015) noticed the shallower slope, i.e., $\alpha \sim -0.1$, for $A_V < 3$ and a very steep slope of $\alpha \sim -2$ for $A_V > 4$. They attributed the enhancement in P_λ/A_V to combined effects of extra radiative torque and H_2 formation torque. The high grain alignment and polarization efficiency in IC 63 also imply the lowest values of rotational damping and enhanced torque due to H_2 formation and due to the presence of anisotropic radiation field compared to the values in the LB. The observed polarization values in IC 59 and IC 63 probe the regions of $A_V < 3.5$, and we obtained the slopes of –0.55 and –0.41 in IC 63 and IC 59, respectively. These

values are in good agreement with the modeled values of Hoang et al. (2015).

5. Summary

We used the optical polarization and multiband photometric observations toward nebulae IC 59 and IC 63 to probe the grain alignment and polarization efficiency. Using the distances to the nebulae and known flux of their illuminating star γ Cas, we have interpreted the results in the context of radiative grain alignment. We compared our results to polarization efficiencies measured in the LB walls (Medan & Andersson 2019). Polarization efficiencies are found to be higher in the IC 59 and IC 63 nebulae than those estimated for the LB. This suggests an enhanced grain alignment due to RAT in these nebulae "because of the close" vicinity of γ Cas compared to the large distances of the walls of LB from OB associations. Because not all grains can cause polarization (due to sphericity, grain mineralogy, etc.), we would expect that there will exist a radiative intensity where the observed linear relationship between polarization efficiency and radiation intensity breaks down. We are currently exploring such extreme environments.

We thank the anonymous referee for very constructive reports that helped significantly improve the content of this paper. The WHT is operated on the island of La Palma by the Isaac Newton Group of Telescopes in the Spanish Observatorio del Roque de Los Muchachos of the Instituto de Astrofísica de Canarias. B-G.A. and A.S. acknowledge the financial support from the NSF through grant AST-1715876. V.S., A.K., and J. Z. acknowledge the financial support from the Research Council of Lithuania, grant No. S-MIP-17-74.

Facilities: WHT, AIMPOL, VATT, Molėtai.

Software: Astropy (Astropy Collaboration et al. 2013), Matplotlib (Hunter 2007), SciPy (Virtanen et al. 2020), NumPy (Harris et al. 2020).

ORCID iDs

Archana Soam https://orcid.org/0000-0002-6386-2906
B-G Andersson https://orcid.org/0000-0001-6717-0686
Miranda Caputo https://orcid.org/0000-0002-2957-3924
R. Janusz https://orcid.org/0000-0001-9146-9274
J. A. Acosta-Pulido https://orcid.org/0000-0002-0433-9656

References

Alves, F. O., Frau, P., Girart, J. M., et al. 2014, A&A, 569, L1
Andersson, B. G., Hoang, T., Lopez-Rodriguez, E., et al. 2018, AAS Meeting, 231, 414.04
Andersson, B.-G., Lazarian, A., & Vaillancourt, J. E. 2015, ARA&A, 53, 501
Andersson, B.-G., Piirola, V., De Buizer, J., et al. 2013, ApJ, 775, 84
Andersson, B.-G., & Potter, S. B. 2007, ApJ, 665, 369
Astropy Collaboration, Robitaille, T. P., Tollerud, E. J., et al. 2013, A&A, 558, A33
Bailer-Jones, C. A. L., Rybizki, J., Fouesneau, M., Mantelet, G., & Andrae, R. 2018, AJ, 156, 58
Berdyugin, A., Piirola, V., & Teerikorpi, P. 2014, A&A, 561, A24
Bhatt, H. C., & Jain, S. K. 1993, A&A, 276, 507
Cashman, L. R., & Clemens, D. P. 2014, ApJ, 793, 126
Chapman, N. L., Goldsmith, P. F., Pineda, J. L., et al. 2011, ApJ, 741, 21
Crutcher, R., Heiles, C., & Troland, T. 2003, in Turbulence and Magnetic Fields in Astrophysics,, ed. E. Falgarone & T. Passot (Berlin: Springer), 155
Cudlip, W., Furniss, I., King, K. J., & Jennings, R. E. 1982, MNRAS, 200, 1169
Dame, T. M., Hartmann, D., & Thaddeus, P. 2001, ApJ, 547, 792
Davis, L. J., & Greenstein, J. L. 1951, ApJ, 114, 206
Dolginov, A. Z., & Mitrofanov, I. G. 1976, Ap&SS, 43, 291
Dotson, J. L., Davidson, J., Dowell, C. D., Schleuning, D. A., & Hildebrand, R. H. 2000, ApJS, 128, 335
Draine, B. T., & Weingartner, J. C. 1996, ApJ, 470, 551
Gendelev, L., & Krumholz, M. R. 2012, ApJ, 745, 158
Hall, J. S. 1949, Sci, 109, 166
Harris, C. R., Millman, K. J., van der Walt, S. J., et al. 2020, Natur, 585, 357
Heyer, M. H., Brunt, C., Snell, R. L., et al. 1998, ApJS, 115, 241
Hiltner, W. A. 1949a, ApJ, 109, 471
Hiltner, W. A. 1949b, Sci, 109, 165
Hoang, T., Lazarian, A., & Andersson, B.-G. 2015, MNRAS, 448, 1178
Hodapp, K.-W. 1987, ApJ, 319, 842
Høg, E., Fabricius, C., Makarov, V. V., et al. 2000, A&A, 355, L27
Hough, J. H., Aitken, D. K., Whittet, D. C. B., Adamson, A. J., & Chrysostomou, A. 2008, MNRAS, 387, 797
Hunter, J. D. 2007, CSE, 9, 90
Jansen, D. J., van Dishoeck, E. F., & Black, J. H. 1994, A&A, 282, 605
Jones, T. J., Bagley, M., Krejny, M., Andersson, B.-G., & Bastien, P. 2015, AJ, 149, 31
Jones, T. J., Klebe, D., & Dickey, J. M. 1992, ApJ, 389, 602
Karr, J. L., Noriega-Crespo, A., & Martin, P. G. 2005, AJ, 129, 954
Kataoka, A., Tsukagoshi, T., Pohl, A., et al. 2017, ApJL, 844, L5
Lallement, R., Vergely, J.-L., Valette, B., et al. 2014, A&A, 561, A91
Lallement, R., Welsh, B. Y., Vergely, J. L., Crifo, F., & Sfeir, D. 2003, A&A, 411, 447
Lazarian, A., & Draine, B. T. 1999, ApJL, 516, L37
Lazarian, A., & Hoang, T. 2007, MNRAS, 378, 910
Lazarian, A., & Hoang, T. 2019, ApJ, 883, 122
Matthews, B. C., McPhee, C. A., Fissel, L. M., & Curran, R. L. 2009, ApJS, 182, 143
Medan, I., & Andersson, B.-G. 2019, ApJ, 873, 87
Navarete, F., Galli, P. A. B., & Damineli, A. 2019, MNRAS, 487, 2771
Pereyra, A., & Magalhães, A. M. 2002, ApJS, 141, 469
Purcell, E. M. 1979, ApJ, 231, 404
Rao, R., Crutcher, R. M., Plambeck, R. L., & Wright, M. C. H. 1998, ApJL, 502, L75
Reid, M. J., Menten, K. M., Zheng, X. W., et al. 2009, ApJ, 700, 137
Serkowski, K. 1973, in IAU Symp. 52, Interstellar Dust and Related Topics, ed. J. M. Greenberg & H. C. van de Hulst (Dordrecht: Reidel), 145
Soam, A., Maheswar, G., Lee, C. W., Neha, S., & Andersson, B. G. 2017, MNRAS, 465, 559
Stil, J., Wityk, N., Ouyed, R., & Taylor, A. R. 2009, ApJ, 701, 330
Straižys, V. 1992, Multicolor Stellar Photometry (Tucson, AZ: Pachart Publishing House)
Straižys, V., Boyle, R. P., Janusz, R., Laugalys, V., & Kazlauskas, A. 2013, A&A, 554, A3
Straižys, V., Boyle, R. P., Milašius, K., et al. 2019, A&A, 623, A22
Sugitani, K., Nakamura, F., Watanabe, M., et al. 2011, ApJ, 734, 63
Vaillancourt, J. E., Andersson, B.-G., Clemens, D. P., et al. 2020, ApJ, 905, 157
Vaillancourt, J. E., & Matthews, B. C. 2012, ApJS, 201, 13
Virtanen, P., Gommers, R., Oliphant, T. E., et al. 2020, NatMe, 17, 261
Vrba, F. J., Strom, S. E., & Strom, K. M. 1976, AJ, 81, 958
Whittet, D. C. B. 2003, Dust in the Galactic Environment (2nd edn.; Bristol: IOP Publishing)
Whittet, D. C. B., Gerakines, P. A., Hough, J. H., & Shenoy, S. S. 2001, ApJ, 547, 872
Wright, C. O., Egan, M. P., Kraemer, K. E., & Price, S. D. 2003, AJ, 125, 359